

Possible Evidence of Thermodynamic Equilibrium in Dark  
Matter Halos

J. Davidson – University of Alabama

S. Sarker – University of Alabama

A. Stern – University of Alabama

Deposited 07/29/2019

Citation of published version:

Davidson, J., Sarker, S., Stern, A. (2014): Possible Evidence of  
Thermodynamic Equilibrium in Dark Matter Halos. *The Astrophysical  
Journal*, 788(1).

DOI: <http://dx.doi.org/10.1088/0004-637X/788/1/37>

## POSSIBLE EVIDENCE OF THERMODYNAMIC EQUILIBRIUM IN DARK MATTER HALOS

JOSHUA DAVIDSON, SANJOY K. SARKER, AND ALLEN STERN

Department of Physics, University of Alabama, Tuscaloosa, AL 35487, USA; jadavidson@crimson.ua.edu, ssarker@ua.edu, astern@ua.edu

Received 2013 February 23; accepted 2014 March 20; published 2014 May 20

### ABSTRACT

After deducing the density profiles and gravitational potential functions of eight galaxies from the rotation velocity data from THINGS, we find that the density decreases exponentially with the potential in substantial regions of the halos. This behavior is in agreement with that of a single-component isothermal Boltzmann gas, and it suggests that an effective description in terms of a Boltzmann gas is possible for dark matter in these regions. This could be an indication that dark matter self-interactions are sufficient in strength and number to lead to thermal equilibrium in these regions. We write down the dynamics and boundary conditions for a Boltzmann gas description and examine some of its qualitative and quantitative consequences. Solutions to the dynamical system are determined by three dimensionfull parameters, and they provide reasonable fits to the rotational velocity data in the regions where the Boltzmann-like behavior was found. Unlike in the usual approach to curve fitting, we do not assume a specific form for the dark matter density profile, and we do not require a detailed knowledge of the baryonic content of the galaxy.

*Key words:* dark matter – galaxies: halos – galaxies: kinematics and dynamics

*Online-only material:* color figures

### 1. INTRODUCTION AND OUTLINE

The paradigm of collisionless cold dark matter has had much success in describing the large scale structure of the universe. Nevertheless, inconsistencies persist with observations at smaller scales. One example is the cusp singularity in the dark matter density profile, which is predicted by simulations of collisionless particles (Navarro et al. 1997) but is in contrast with observations, in particular, for dwarf galaxies (Oh et al. 2011; Frusciante et al. 2012). The possibility that such inconsistencies may be cured with the inclusion of non-gravitational self-interactions was suggested a number of years ago (Spergel & Steinhardt 2000; Dave et al. 2001). The proposal of self-interacting dark matter (having interaction times less than the Hubble time) is not currently excluded, despite existing constraints on the interactions coming from halo shapes and cluster interactions. Numerous models for dark matter self-interactions have been considered, and their role in curing observational anomalies has been explored (Mohapatra et al. 2002; Foot & Volkas 2004; Ackerman et al. 2009; Buckley & Fox 2010; Feng et al. 2010; Chang et al. 2010; Loeb & Weiner 2011; Lin et al. 2012; Tulin et al. 2013a, 2013b; Kaplinghat et al. 2013; Destri et al. 2013). Since self-interactions among dark matter particles are not excluded, it is then reasonable to ask whether conditions may be suitable in galaxies for a gas of dark matter particles to reach a state of thermodynamic equilibrium. From the theoretical side, it is a non-trivial problem to know precisely what conditions should be satisfied for this to occur since the nature of the interaction is unknown. However, it is possible to search for indications of thermal equilibrium in regions of galactic halos from direct observations. This can be done using the rotation curve data, which is a central theme of the article.

Our paper contains two parts. In the first part (Section 2), we search for regions in galactic halos that show behavior which is analogous to what one would expect from a classical (Boltzmann) gas in thermal equilibrium. In addressing this issue, we only need to require that the region of interest in the halo is approximately spherically symmetric and that the

source of the rotation curves are circular orbits. Both of these assumptions are commonly utilized in curve fittings of the rotation velocity data. With these two assumptions, one can simultaneously determine the halo density  $\rho$  and gravitational potential  $\phi$  from orbital speeds of H I gas in the halo. The assumption of spherical symmetry means that these quantities are functions of a single parameter. Rather than taking the parameter to be the radial coordinate  $r$ , we can write  $\rho$  as a function of  $\phi$ . (This is a single-valued function because  $\phi$  monotonically increases with  $r$ .) It is then of interest to search for some universal behavior for  $\rho(\phi)$ . In particular, an exponentially decreasing function would indicate agreement with a self-interacting classical gas in thermodynamic equilibrium. To be more specific, the determination of  $\phi(r)$  and  $\rho(r)$  from the circular orbital speed  $v(r)$  follows from simple classical physics considerations. The former is obtained by integrating Newton's law,

$$\frac{d\phi}{dr} = \frac{v^2(r)}{r}, \quad (1)$$

while the latter comes from the Poisson equation,  $\nabla^2\phi = 4\pi G\rho(r)$ , with  $G$  being the gravitational constant. Upon assuming spherical symmetry and then substituting (1) one gets

$$\rho(r) = \frac{1}{4\pi Gr^2} \frac{d}{dr}(rv^2(r)). \quad (2)$$

From  $\phi(r)$  and  $\rho(r)$ , we then obtain  $\rho(\phi)$ .

Before discussing analysis of the rotation curve data, it is useful to make a few remarks about the ideal case of *exactly* flat rotation curves, i.e.,  $v(r) = \text{constant}$ .  $\phi$  varies logarithmically in  $r$  in this case, while from (2), one gets that  $\rho(r) \propto 1/r^2$ . It is a well-known curiosity that the combination of these two results gives an exponential behavior for  $\rho(\phi)$ , i.e.,  $\rho(\phi) \propto e^{-\phi/\phi_0}$ , where  $\phi_0$  is a constant associated with the so-called velocity dispersion. Therefore, the source of the gravitational potential responsible for exactly flat rotation curves behaves in an identical manner to a single component isothermal Boltzmann gas.

Of course, a galactic system is not a single component system, and the density and gravitational potential get contributions from both dark matter and baryonic matter. Moreover, the above scenario is an oversimplification, since in nature, rotation curves are not exactly flat. On the other hand, the absence of exactly flat rotation curves from galaxies does not rule out an exponential behavior for  $\rho(\phi)$ . For that reason, it is of interest to make a more accurate determination of  $\rho(\phi)$  from the rotation curves in the galactic halos. We do so using the data from THINGS (de Blok et al. 2008). A local maximum can be identified for most of the rotation curves. So for them, there is always a small neighborhood where  $v$  is approximately constant, and it would come as no surprise to find that  $\rho$  decreases exponentially with  $\phi$  in that neighborhood. A more significant result would be to find exponential behavior for  $\rho(\phi)$  in a region that extends far beyond a local maximum. We present evidence that this is the case for 8 galaxies (out of 19) in the THINGS survey. They are NGC 2841, NGC 5055, NGC 7331, NGC 2403, NGC 2903, NGC 3521, NGC 3198, and DD0 154. The results suggest that an effective Boltzmann gas description of dark matter is possible for certain regions of galactic halos or, more precisely, spherical shells  $R_G \leq r \leq R_{\max}$ . The constant  $1/\phi_0$  can be approximately determined for these regions, which can then be identified with the ratio of particle mass  $m$  with some effective temperature  $T$  (times Boltzmann’s constant  $k_B$ ). In Section 2, we estimate  $m/T$  for the eight galaxies in the relevant regions.

In the second part of the paper, beginning with Section 3, we make a model utilizing the effective Boltzmann description. The dynamics of the model is taken to be that of a single-component self-gravitating isothermal gas, which is assumed to be valid for the spherical shell,  $R_G \leq r \leq R_{\max}$ . Along with spherical symmetry, the model makes the simplifying assumption that only dark matter is present at distances larger than  $R_G$  and that all baryonic matter is contained within a sphere of radius  $R_G$ . (Dark matter is also assumed to be present for  $r < R_G$ .) The baryonic component nevertheless strongly influences the region of interest  $R_G \leq r \leq R_{\max}$ , as it contributes to the gravitational acceleration  $\frac{d\phi}{dr}$ , and thus is responsible for a tidal force on the isothermal gas. The pressure balance implicitly holds everywhere within and beyond the isothermal region, with the pressure within the isothermal region given by the ideal gas equation.

The relevant dynamical equation for such a system has been known for a long time (Emden 1907). It is the Emden equation, which is just the Poisson equation with an isothermal Boltzmann gas source. It has a well-known solution, found by Emden, which satisfies the condition that it be nonsingular for *all* values of the radial coordinate,  $0 \leq r < \infty$ . The solution results from the boundary condition that states that the gravitational force vanishes at the origin. Emden’s solution gives a unique density profile and yields a flat rotation curve in the asymptotic limit  $r \rightarrow \infty$ .

Since for us the relevant domain is a spherical shell, the condition that the solution be nonsingular for all  $r$  is too restrictive, and we must seek alternative boundary conditions, and hence alternative solutions. The appropriate conditions for our case should be imposed at the inner boundary,  $r = R_G$ . The derivative of  $\phi$  at this point gives the gravitational attraction to the matter in the interior region  $r < R_G$ . The baryonic component dominates the interior region, and so it is largely responsible for the boundary conditions at  $r = R_G$ , and it contributes to the gravitational potential of the Boltzmann gas. In Section 3, we show that a family of spherically symmetric

solutions to the Emden equations results from such boundary conditions. They then lead to a family of density profiles that are parameterized by two dimensionless constants, which we denote by  $\kappa$  and  $\tau$ . The parameters can be expressed as functions of the total mass  $M_G$  in the interior region  $r < R_G$ , as well as  $R_G$  and the effective temperature of the gas. The family of solutions contains Emden’s solution as a special case. Another special solution is one which gives an exactly flat rotation curve for all of  $R_G \leq r \leq R_{\max}$ .<sup>1</sup> It results from particular values of the two dimensionless parameters  $\kappa$  and  $\tau$ . Since the solution yields an exactly flat rotation curve, it should serve as a crude fit to observations. From the crude fit one can determine the ratio  $m/T$  in terms of the orbital speed in the halo. For instance, from typical orbital speeds of  $\sim 200 \text{ km s}^{-1}$ , one gets  $m/T \sim 400 \text{ eV K}^{-1}$ . If one takes the analogy with the Boltzmann gas further and regards  $T$  as the temperature of a gas in equilibrium, the equipartition theorem for this system implies that the mean speed of the dark matter particles in the gas is of the same order of magnitude as the rotational speed for H I in the halo. So if the orbital speed is a few hundred  $\text{km s}^{-1}$ , the speed of the particles in the gas is also a few hundred  $\text{km s}^{-1}$ , and this result is independent of the dark matter mass. Details of this argument are given in Section 3.

We go beyond the crude approximation in Section 4. There we perform fits of the rotation curve data to the solutions of the self-gravitating isothermal gas for the eight galaxies examined in Section 2. The fits are applied only to the regions  $R_G \leq r \leq R_{\max}$  of the halos where  $\rho(\phi)$  exhibited exponential behavior. Our approach is quite different from the usual approach to curve fitting, such as Navarro–Frenk–White (NFW) fits (Navarro et al. 1997). We do not assume any specific form for the dark matter density profile. Rather, the density  $\rho(r)$  is inferred from the fitted solution. We also do not require any detailed knowledge of the baryonic content of the galaxy. These details are often difficult to accurately determine, yet they play a crucial role in the usual approach to curve fitting. Moreover, results differ significantly from one mass model to another. In the usual approach to curve fitting, the matter contributions from the disk, bulge, and H I gas must be subtracted from the rotation curve data. Here, on the other hand, it would be a mistake to subtract off the baryonic contribution to the rotation velocity before doing the curve fitting. This is because the contribution of baryonic matter from the inner region  $r \leq R_G$  is already included in the gravitational potential  $\phi(r)$ . Moreover, the Boltzmann equation determines the actual rotational velocity, not the individual contributions from the different components. Finally, while fits to rotational curve data are usually performed for the entire galaxy, here it makes sense to perform the fits to the Boltzmann gas only for the spherical shell,  $R_G \leq r \leq R_{\max}$ , where evidence for such a behavior has been found from the data.

While only two dimensionless parameters are needed to specify solutions to the Boltzmann equation, three *dimensionfull* parameters are required to fit the rotational velocity data. They are  $m/T$ , the density  $\rho(R_G)$  at  $r = R_G$ , and the total mass  $M(R_G)$  contained inside the sphere of radius  $R_G$ . Not too surprisingly, the result for  $m/T$  obtained from the fit are reasonably consistent with the corresponding values obtained in Section 2. We use the fit to estimate the mass  $M_{(R_G, R_{\max})}$  of the region  $R_G \leq r \leq R_{\max}$  exhibiting the Boltzmann behavior. In most cases, we find that this mass is larger than the inner region  $r < R_G$ . We also find that

<sup>1</sup> This solution has often been referred to as the “singular” isothermal sphere because it is singular in the limit  $r = 0$ . For us, however, the solution is *nonsingular* because the origin is excluded from the domain.

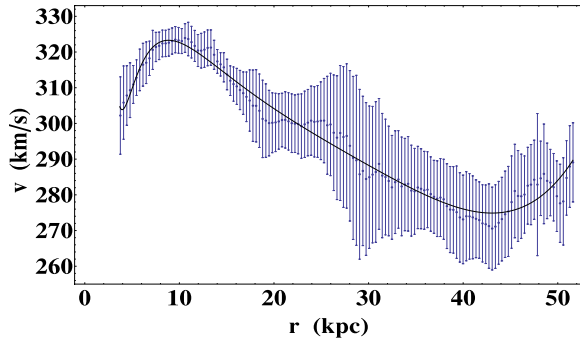


**Figure 1.** Eight-parameter series fit of rotation velocity data for NGC 2841 from  $r = 3.8$  to 51.6 kpc.

(A color version of this figure is available in the online journal.)

in most cases,  $M_{(R_G, R_{\max})}$  is larger than previous estimates of the total baryonic mass of the galaxy, obtained from mass models (de Blok et al. 2008). This lends support to the conclusion that the region  $R_G \leq r \leq R_{\max}$  exhibiting Boltzmann-like behavior contains a significant fraction of the total mass of the galaxy, and that it consists primarily of dark matter.

A summary of the results for the eight galaxies, including two tables, is given in Section 5, along with concluding remarks.

## 2. DETERMINATION OF $\rho(\phi)$ FROM ROTATION CURVE DATA

As stated in the introduction, the density function  $\rho(r)$  and gravitational potential  $\phi(r)$  in the halo can be numerically determined from the rotation velocity data under certain simplifying assumptions. The assumptions are that the system is spherically symmetric and that the rotation velocity data are attributed to circular orbits.  $\phi(r)$  and  $\rho(r)$  are obtained from  $v(r)$  using Equations (1) and (2), respectively. The two functions can then be combined to determine  $\rho(\phi)$ . In order to search for Boltzmann-like behavior, it is useful to plot  $\log \rho$  versus  $\phi$ . We do this for the eight mentioned galaxies in the THINGS survey. Boltzmann-like behavior would correspond to a straight line with negative slope in the plot of  $\log \rho$  versus  $\phi$ , the slope being  $\phi_0$  or  $T/m$ . We also plot  $-(d/d\phi)\log \rho$  versus  $r$  for the eight galaxies. Boltzmann-like behavior would yield a constant in the latter graph, corresponding to the value of  $m/T$  for the gas.

The first step in the analysis is to fit the rotation velocity data to a smooth curve  $v(r)$ . We should mention that the results for  $\rho(\phi)$  are somewhat sensitive to how closely one fits the data to a smooth curve. In order to reduce the subjectivity of the analysis, we fit all eight galaxies in the sample to the same eight-parameter series, i.e.,  $\sum_{n=-3}^4 a_n r^n$ . Our analysis reveals an exponential behavior for regions of the halos. This behavior becomes less evident if we make a cruder fit to the data, using only a few parameters. On the other side, additional features of the halo obscure the exponential behavior if one includes too many parameters.

The eight galaxies are organized into four categories: unbarred galaxies (NGC 2841, NGC 5055, and NGC 7331), weakly barred galaxies (NGC 2403, NGC 2903, and NGC 3521), a barred spiral galaxy (NGC 3198), and, finally, a dwarf galaxy (DD0 154).

We begin with the unbarred galaxies. After first listing some relevant information for these galaxies, we then determine  $\log(\rho(\phi))$  from the data.

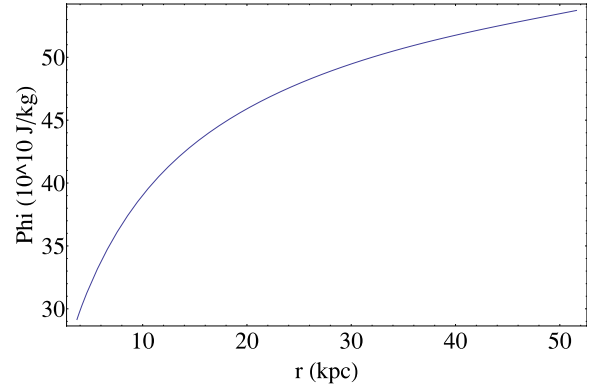


**Figure 2.** Resulting gravitational potential vs.  $r$  for NGC 2841 from  $r = 3.8$  to 51.6 kpc. The zero of the potential is at  $r = 3.8$ .

(A color version of this figure is available in the online journal.)

### 2.1. NGC 2841

The morphology classification of NGC 2841 is SA(r)b. It is a flocculent, unbarred giant spiral galaxy, with a classical bulge and a significant population of blue stars. A certain mass model gives the disk and bulge masses for NGC 2841 of  $1.096 \times 10^{11} M_\odot$  and  $2.51 \times 10^{10} M_\odot$ , respectively.<sup>2</sup> Using Mannheim & O'Brien (2012), the distance scale of the disk is  $\sim 3.5$  kpc. The H I gas mass for NGC 2841 is  $8.6 \times 10^9 M_\odot$  (Walter et al. 2008). This is approximately 6% of the disk plus bulge mass, so one would expect it to make only a small contribution to the total density in the halo. More background information about NGC 2841 can be found in de Blok et al. (2008).

The THINGS rotation velocity data for NGC 2841 is available at distances up to 51.6 kpc, or almost 15 times the distance scale of the disk. Figure 1 shows an eight-parameter fit of the rotation velocity data to the series  $\sum_{n=-3}^4 a_n r^n$  from  $r = 3.8$  to 51.6 kpc. The fit is done to the midpoints (corresponding to the dots) of the error bars. From the fitted function for  $v(r)$ , we obtain the gravitational potential  $\phi(r)$  by numerically integrating Equation (1). The result is shown in Figure 2. The density profile  $\rho(r)$  is found using Equation (2) and is shown in Figure 3.<sup>3</sup> The latter two plots are combined in Figure 4 to give  $\log(\rho(r)/\rho_0)$  versus  $\phi(r)$ , where  $\rho_0$  is a constant with units of density. It approximately coincides with a straight line with negative slope in the region  $7 < r < 22$  kpc. From this figure, it is evident that  $\rho(\phi)$  has an exponential behavior in the region  $7 < r < 22$  kpc, or approximately from 2 to 6 times the distance scale of the disk. Finally, in Figure 5, we plot minus the derivative of  $\log \rho$  with  $\phi$  versus  $r$ . An approximately constant value of  $\sim 190 \text{ eV K}^{-1}$  is obtained for  $-(d \log \rho / d\phi)$  over the range  $7 < r < 22$  kpc, which is shown in the inset. Therefore, this region is consistent with the description of

<sup>2</sup> More specifically, these values were obtained using models with fixed values of the mass-to-luminosity ratio and the de Salpeter stellar initial mass function. (They were obtained from Table 3 of de Blok et al. 2008.) As we indicated previously, the baryonic masses for any given galaxy differ significantly from one model to another. These details play no direct role in the analyses we do here.

<sup>3</sup> Figure 3 exhibits a region beyond 40 kpc where the density increases with increasing  $r$ . Similar results are seen for very distant regions of NGC 7331, NGC 2903, NGC 3521, and NGC 3198. This behavior is presumably unphysical, so if one can trust the fits in these regions, it may indicate that the two assumptions (spherical symmetry and circular orbits) used in obtaining  $\rho(r)$  are invalid for these particular regions. In any case, these regions are far beyond the domains of interest in our paper, which exhibit Boltzmann-like behavior.

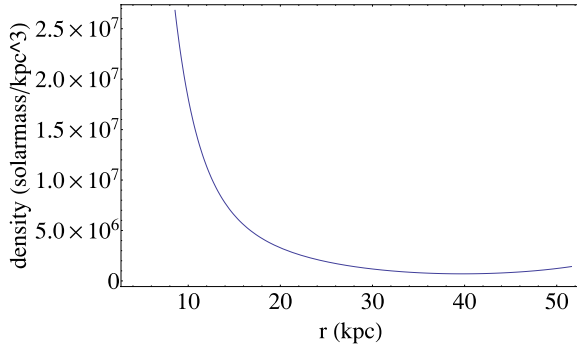


**Figure 3.** Resulting density vs.  $r$  for NGC 2841 from  $r = 3.8$  to  $51.6$  kpc. (A color version of this figure is available in the online journal.)

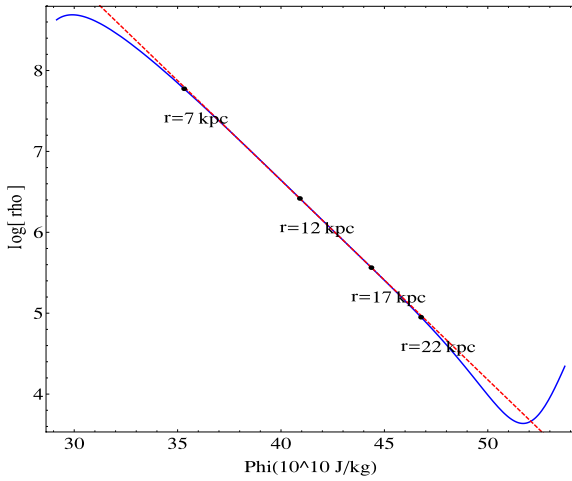


**Figure 4.**  $\log(\text{density}/\text{constant})$  vs. the gravitational potential for NGC 2841 for  $r = 3.8$  to  $51.6$  kpc. It is compared to a straight line (red, dashed) with slope  $\approx -190$  eV  $\text{K}^{-1}$ . The two plots approximately coincide for  $7 < r < 22$  kpc. (A color version of this figure is available in the online journal.)

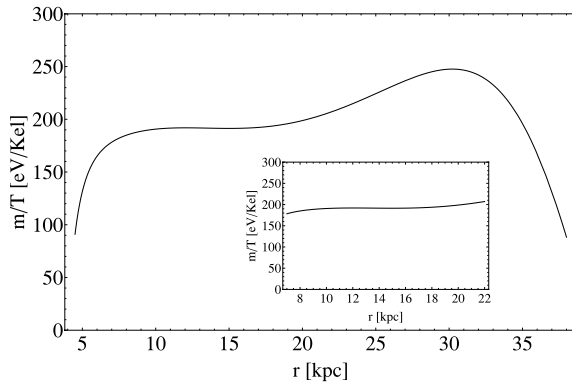


**Figure 5.**  $-(d \log \rho / d \phi)$  vs.  $r$  for NGC 2841. The plot is approximately constant for the domain  $7 < r < 22$  kpc, which is shown in the inset.

a Boltzmann gas with  $m/T \sim 190$  eV  $\text{K}^{-1}$ .  $-(d \log \rho / d \phi)$  gradually increases to  $\sim 250$  eV  $\text{K}^{-1}$  over the range  $20 < r < 30$  kpc, before rapidly decreasing beyond 30 kpc.

## 2.2. NGC 5055

The morphology classification of NGC 5055 is SA(rs)bc. It is an unbarred spiral galaxy with an extended warp at end of the optical disk. It has a regular structure with well-defined flocculent spiral arms and is part of the M51 group of galaxies. Mass models (see de Blok et al. 2008) give the

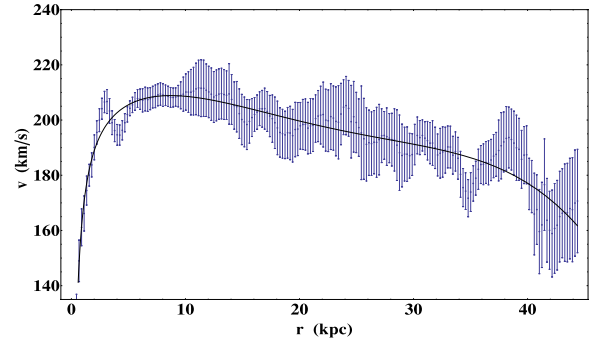


**Figure 6.** Series fit of rotation velocity data for NGC 5055 from  $r = 0.2$  to  $44.4$  kpc.

(A color version of this figure is available in the online journal.)

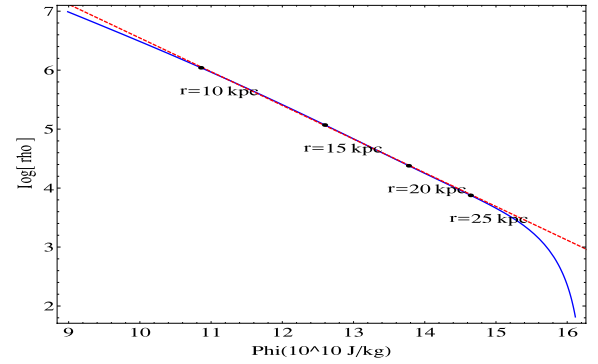


**Figure 7.**  $\log(\text{density}/\text{constant})$  vs. the gravitational potential for NGC 5055 for  $r = 6.5$  to  $37.5$  kpc. It is compared to a straight line (red, dashed) with slope  $\approx -440$  eV  $\text{K}^{-1}$ . The two plots approximately coincide for  $10 < r < 25$  kpc.

(A color version of this figure is available in the online journal.)

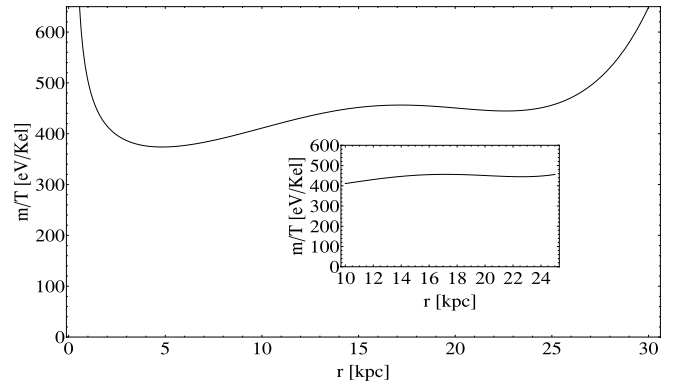


**Figure 8.**  $-(d \log \rho / d \phi)$  vs.  $r$  for NGC 5055. The plot is approximately constant for the domain  $10 < r < 25$  kpc, which is shown in the inset.

disk and bulge masses for NGC 5055 of  $1.203 \times 10^{11} M_{\odot}$  and  $2.09 \times 10^9 M_{\odot}$ . The distance scale of the disk is  $\sim 3.622$  kpc (Mannheim & O'Brien 2012). The H I gas mass for NGC 5055 is  $0.91 \times 10^{10} M_{\odot}$  (Walter et al. 2008), which is approximately 7% of the disk plus bulge mass.

THINGS rotation velocity data are available at distances up to  $\sim 44.4$  kpc, around 12 times the distance scale of the disk. An eight-parameter series fit, again using  $\sum_{n=-3}^4 a_n r^n$ , of the data from  $r = 0.2$  to  $44.4$  kpc appears in Figure 6. Here we do not include a plot of  $\phi(r)$  and  $\rho(r)$ , but we give the plot of  $\log(\rho(r)/\text{constant})$  versus  $\phi(r)$  in Figure 7. An approximate straight line with negative slope is recovered upon restricting the radial coordinate to  $10 < r < 25$  kpc. In Figure 8, we plot

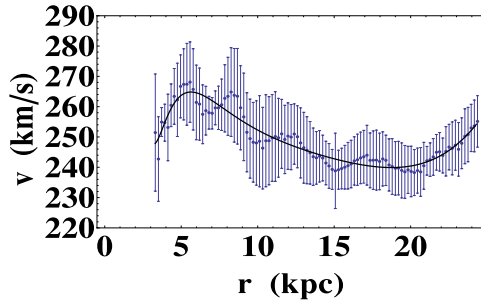


**Figure 9.** Series fit of rotation velocity data for NGC 7331 from  $r = 3.3$  to 24.4 kpc.

(A color version of this figure is available in the online journal.)

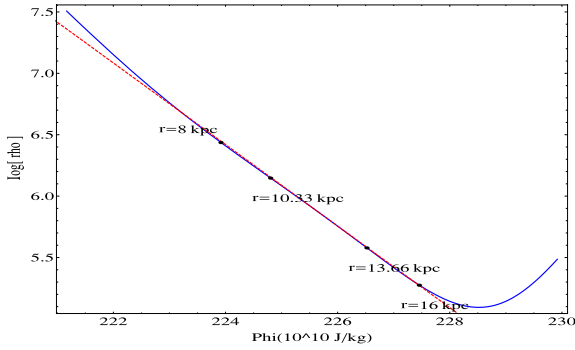


**Figure 10.**  $\log(\text{density}/\text{constant})$  vs. the gravitational potential for NGC 7331 for  $r = 6$  to 24.3 kpc. It is compared to a straight line (red, dashed) with slope  $\approx -260 \text{ eV K}^{-1}$ . The two plots approximately coincide for  $8 < r < 16$  kpc.

(A color version of this figure is available in the online journal.)

minus the derivative of  $\log \rho$  with  $\phi$  versus  $r$ . It is approximately constant in the domain  $10 < r < 25$  kpc (shown in the inset), with an average value of  $\sim 440 \text{ eV K}^{-1}$ .  $-(d \log \rho / d\phi)$  reaches a minimum value of  $\sim 375 \text{ eV K}^{-1}$  at  $r \approx 4$  kpc, before rapidly increasing at smaller distances.

### 2.3. NGC 7331

The morphology classification of NGC 7331 is SA(s)b. It is regular at large scales, but spiral arms cause wiggles in velocity contours; and there are large differences in the rotation curve for the approaching and receding sides (de Blok et al. 2008). Mass models give the disk and bulge masses for NGC 7331 of  $1.66 \times 10^{11} M_{\odot}$  and  $1.74 \times 10^{10} M_{\odot}$ . The distance scale of the disk is  $\sim 3.2$  kpc (Mannheim & O'Brien 2012). The H I gas mass for NGC 7331 is  $.91 \times 10^{10} M_{\odot}$  (Walter et al. 2008), which is approximately 5% of the disk plus bulge mass.

THINGS rotation velocity data are available at distances up to  $\sim 24.4$  kpc, or over seven times the distance scale of the disk. The eight-parameter series fit of rotation velocity data from  $r = 3.3$  to 24.4 kpc appears in Figure 9. The resulting plot of  $\log(\rho(r)/\text{constant})$  versus  $\phi(r)$  is given in Figure 10. An approximate straight line with negative slope is recovered upon restricting the radial coordinate to  $8 < r < 16$  kpc. In Figure 11, we plot minus the derivative of  $\log \rho$  with  $\phi$  versus  $r$ . It is approximately constant in the domain  $8 < r < 16$  kpc (shown in the inset), with an average value of  $\sim 260 \text{ eV K}^{-1}$ .  $-(d \log \rho / d\phi)$  reaches a maximum value of  $\sim 340 \text{ eV K}^{-1}$  at  $r \approx 5.5$  kpc.

Next, we repeat the previous analysis for weakly barred spiral galaxies: NGC 2403, NGC 2903, and NGC 3521.

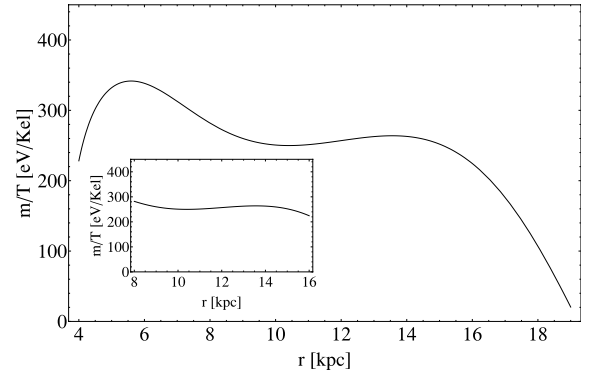


**Figure 11.**  $-(d \log \rho / d\phi)$  vs.  $r$  for NGC 7331. The plot is approximately constant over the domain  $8 < r < 16$  kpc, which is shown in the inset.

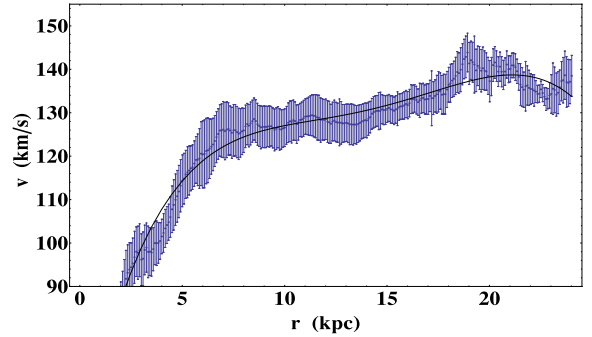


**Figure 12.** Eight-parameter series fit of rotation velocity data for NGC 2403 from  $r = 0.1$  to 24 kpc.

(A color version of this figure is available in the online journal.)

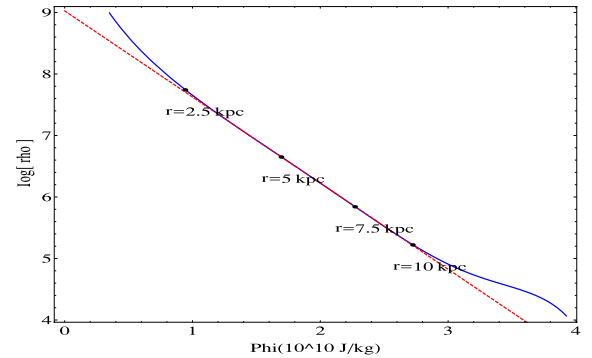


**Figure 13.**  $\log(\text{density}/\text{constant})$  vs. the gravitational potential for NGC 2403 for  $r = 1$  to 20 kpc. It is compared to a straight line (red, dashed) with slope  $\approx -1100 \text{ eV K}^{-1}$ . The two plots approximately coincide for  $3 < r < 10$  kpc.

(A color version of this figure is available in the online journal.)

### 2.4. NGC 2403

The morphology classification of NGC 2403 is SAB(s)cd. Mass models (see de Blok et al. 2008) give the disk and bulge masses for NGC 2403 of  $4.68 \times 10^9 M_{\odot}$  and  $4.27 \times 10^8 M_{\odot}$ , respectively. The distance scale of the disk is  $\sim 2.7$  kpc (Mannheim & O'Brien 2012). The H I gas mass for NGC 2403 is  $2.58 \times 10^9 M_{\odot}$  (Walter et al. 2008), which is approximately 50% of the disk plus bulge mass.

THINGS rotation velocity data are available at distances up to  $\sim 24$  kpc, or almost nine times the distance scale of the disk. The eight-parameter series fit of rotation velocity data from  $r = 0.1$  to 24 kpc appears in Figure 12. The resulting plot of  $\log(\rho(r)/\text{constant})$  versus  $\phi(r)$  is given in Figure 13.

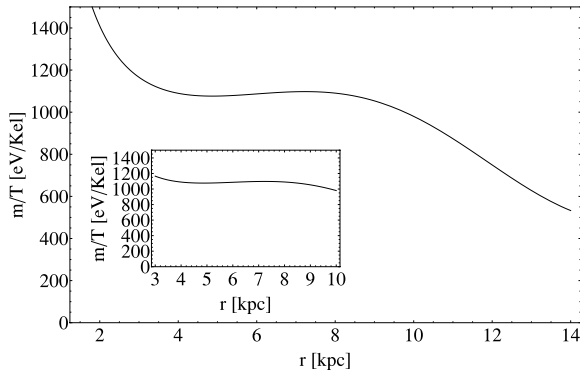


**Figure 14.**  $-(d \log \rho / d \phi)$  vs.  $r$  for NGC 2403. The plot is approximately constant over the domain  $3 < r < 10$  kpc, which is shown in the inset.

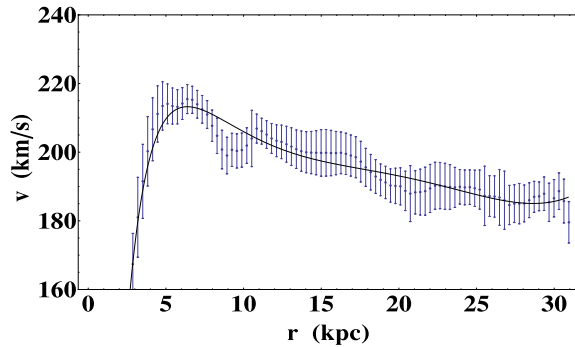


**Figure 15.** Series fit of rotation velocity data for NGC 2903 from  $r = 0.3$  to 31 kpc.

(A color version of this figure is available in the online journal.)

An approximate straight line with negative slope is recovered upon restricting the radial coordinate to  $3 < r < 10$  kpc. In Figure 14, we plot minus the derivative of  $\log \rho$  with  $\phi$  versus  $r$ . It is approximately constant in the domain  $3 < r < 10$  kpc (shown in the inset), with an average value of  $\sim 1100 \text{ eV K}^{-1}$ .

### 2.5. NGC 2903

The morphology classification of NGC 2903 is SAB(rs)bc. It has tightly wound spiral arms. Mass models (see de Blok et al. 2008) give the disk and bulge masses for NGC 2903 of  $1.41 \times 10^{10} M_{\odot}$  and  $2.14 \times 10^9 M_{\odot}$ , respectively. The distance scale of the disk is  $\sim 3.0$  kpc (Mannheim & O'Brien 2012). The H I gas mass for NGC 2903 is  $4.35 \times 10^9 M_{\odot}$  (Walter et al. 2008), which is approximately 27% of the disk plus bulge mass.

THINGS rotation velocity data are available at distances up to 31 kpc, which is over ten times the distance scale of the disk. An eight-parameter series fit of rotation velocity data from  $r = 0.3$  to 31 kpc appears in Figure 15. The resulting plot of  $\log(\rho(r)/\text{constant})$  versus  $\phi(r)$  is given in Figure 16. An approximate straight line with negative slope is recovered upon restricting the radial coordinate to  $3 < r < 9$  kpc. In Figure 17, we plot minus the derivative of  $\log \rho$  with  $\phi$  versus  $r$ . It is approximately constant in the domain  $3 < r < 9$  kpc (shown in the inset), with an average value of  $\sim 490 \text{ eV K}^{-1}$ . If one extends the domain up to 25 kpc, the value of  $m/T$  varies from  $\sim 350$  to  $\sim 650 \text{ eV K}^{-1}$ .

### 2.6. NGC 3521

The morphology classification of NGC 3521 is SAB(rs)bc. It has a flocculent spiral structure and a negligible bulge.

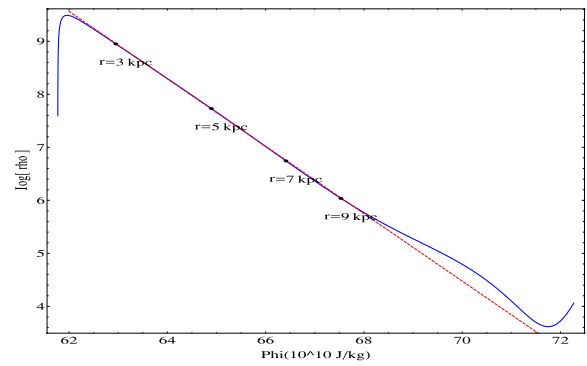


**Figure 16.**  $\log(\text{density}/\text{constant})$  vs. the gravitational potential for NGC 2903 for  $r = 1$  to 31 kpc. It is compared to a straight line (red, dashed) with slope  $\approx -490 \text{ eV K}^{-1}$ . The two plots approximately coincide for  $3 < r < 9$  kpc.

(A color version of this figure is available in the online journal.)

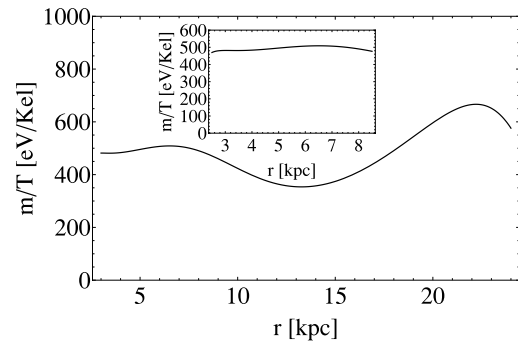


**Figure 17.**  $-(d \log \rho / d \phi)$  vs.  $r$  for NGC 2903. The plot is approximately constant over the domain  $3 < r < 9$  kpc, which is shown in the inset.

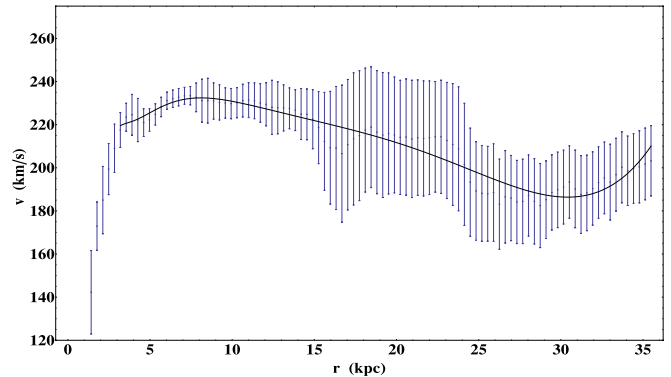


**Figure 18.** Series fit of rotation velocity data for NGC 3521 from  $r = 3.2$  to 35.5 kpc.

(A color version of this figure is available in the online journal.)

Mass models (see de Blok et al. 2008) give the disk mass for NGC 3521 of  $1.23 \times 10^{11} M_{\odot}$ , with a corresponding distance scale of  $\sim 3.3$  kpc (Mannheim & O'Brien 2012). The H I gas mass for NGC 3521 is  $0.802 \times 10^{10} M_{\odot}$  (Walter et al. 2008), which is approximately 6.5% of the disk mass.

THINGS rotation velocity data are available at distances up to 35.5 kpc, which is over 10 times the distance scale of the disk. An eight-parameter series fit of rotation velocity data from  $r = 3.2$  to 35.5 kpc appears in Figure 18. The resulting plot of  $\log(\rho(r)/\text{constant})$  versus  $\phi(r)$  is given in Figure 19. An approximate straight line with negative slope is recovered upon restricting the radial coordinate to  $7 < r < 15$  kpc. In Figure 20, we plot minus the derivative of  $\log \rho$  with  $\phi$  versus  $r$ . It is approximately constant in the domain  $7 < r < 15$  kpc (shown

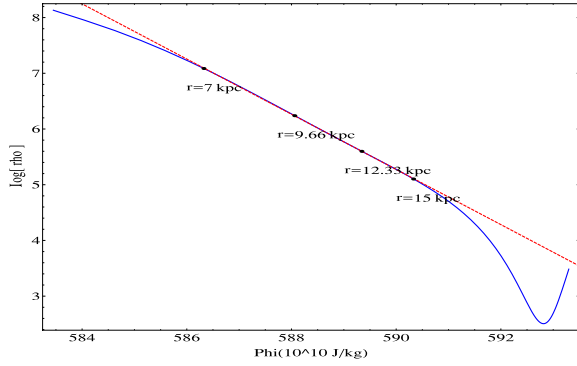


**Figure 19.**  $\log(\text{density}/\text{constant})$  vs. the gravitational potential for NGC 3521 for  $r = 4$  to 30 kpc. It is compared to a straight line (red, dashed) with slope  $\approx -380 \text{ eV K}^{-1}$ . The two plots approximately coincide for  $7 < r < 15$  kpc.

(A color version of this figure is available in the online journal.)

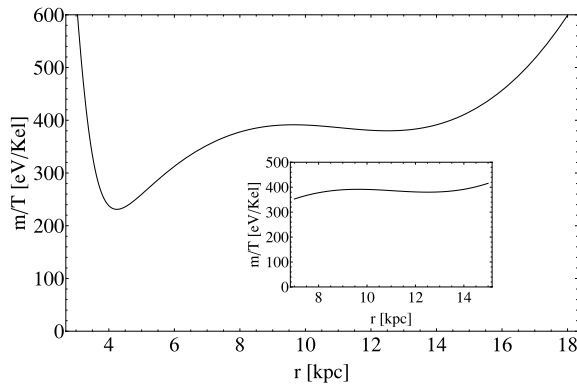


**Figure 20.**  $-(d \log \rho / d \phi)$  vs.  $r$  for NGC 3521. The plot is approximately constant over the domain  $7 < r < 15$  kpc, which is shown in the inset.

in the inset), with an average value of  $\sim 380 \text{ eV K}^{-1}$ . A minimum of  $\sim 230 \text{ eV K}^{-1}$  occurs at  $\sim 4$  kpc.

We next consider the barred spiral galaxy NGC 3198.

### 2.7. NGC 3198

The morphology classification of NGC 3198 is SB(rs)c. This galaxy has two well-defined spiral arms and has indications of a modest warp. Mass models (see de Blok et al. 2008) give the disk and bulge masses for NGC 3198 of  $2.82 \times 10^{10} M_{\odot}$  and  $2.88 \times 10^9 M_{\odot}$ , respectively. The distance scale of the disk is  $\sim 4.0$  kpc (Mannheim & O'Brien 2012). The H I gas mass for NGC 3198 is  $1.017 \times 10^{10} M_{\odot}$  (Walter et al. 2008), which is approximately 33% of the disk plus bulge mass.

THINGS rotation velocity data are available at distances up to 38.5 kpc, which is over nine times the distance scale of the disk. The eight-parameter series fit of rotation velocity data from  $r = 4.1$  to 38.5 kpc appears in Figure 21. The resulting plot of  $\log(\rho(r)/\text{constant})$  versus  $\phi(r)$  is given in Figure 22. An approximate straight line with a negative slope is recovered upon restricting the radial coordinate to  $5 < r < 15$  kpc. In Figure 23, we plot minus the derivative of  $\log \rho$  with  $\phi$  versus  $r$ . It ranges between  $\sim 750 \text{ eV K}^{-1}$  and  $\sim 950 \text{ eV K}^{-1}$  and has an average value of  $\sim 820 \text{ eV K}^{-1}$  for the domain  $5 < r < 25$  kpc.

Finally, we repeat the analysis for the dwarf galaxy DD0 154.

### 2.8. DD0 154

The morphology classification of DD0 154 is IB(s)m. It is a gas-rich dwarf irregular galaxy with a negligible bulge. Mass models (see de Blok et al. 2008) give the disk mass for DD0

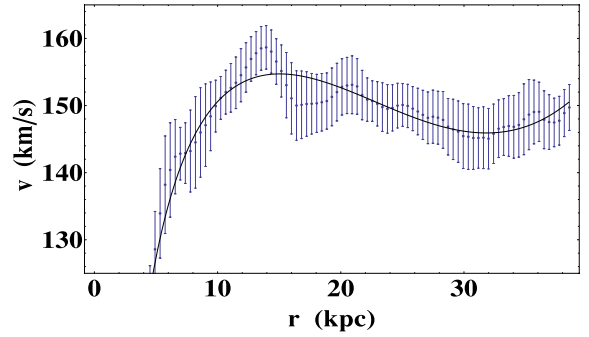


**Figure 21.** Eight-parameter series fit of rotation velocity data for NGC 3198 from  $r = 4.1$  to 38.5 kpc.

(A color version of this figure is available in the online journal.)

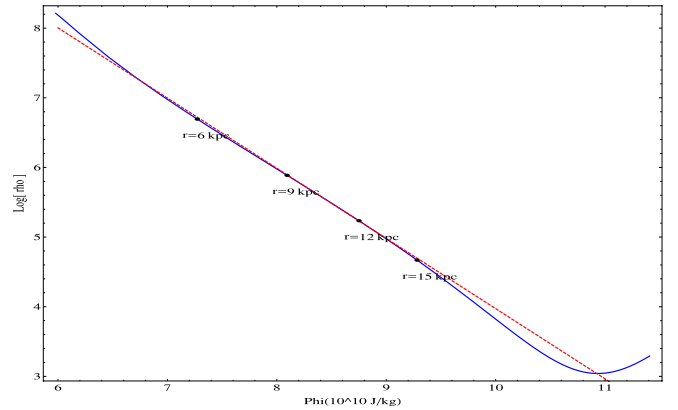


**Figure 22.**  $\log(\text{density}/\text{constant})$  vs. the gravitational potential for NGC 3198 for  $r = 2$  to 39.5 kpc. It is compared to a straight line (red, dashed) with slope  $\approx -820 \text{ eV K}^{-1}$ . The two plots approximately coincide for  $5 < r < 15$  kpc.

(A color version of this figure is available in the online journal.)

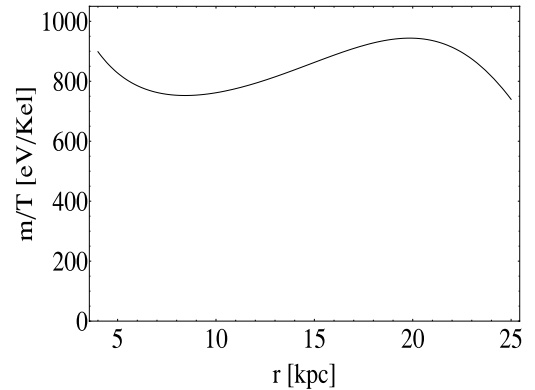


**Figure 23.**  $-(d \log \rho / d \phi)$  vs.  $r$  for NGC 3198. The plot ranges between  $\sim 750 \text{ eV K}^{-1}$  and  $\sim 950 \text{ eV K}^{-1}$  for the domain  $5 < r < 25$  kpc.

154 of  $2.63 \times 10^7 M_{\odot}$ , with a corresponding distance scale of  $\sim 0.8$  kpc (Mannheim & O'Brien 2012). The H I gas mass for DD0 154 is  $3.58 \times 10^8 M_{\odot}$  (Walter et al. 2008), which is approximately 13.6 times the disk mass.

THINGS rotation velocity data are available at distances up to 8 kpc, or 10 times the distance scale of the disk. The eight-parameter series fit of rotation velocity data from  $r = 0.3$  to 8 kpc appears in Figure 24. The resulting plot of  $\log(\rho(r)/\text{constant})$  versus  $\phi(r)$  is given in Figure 25. An approximate straight line with negative slope is recovered upon restricting the radial coordinate to  $1.5 < r < 4.5$  kpc. In

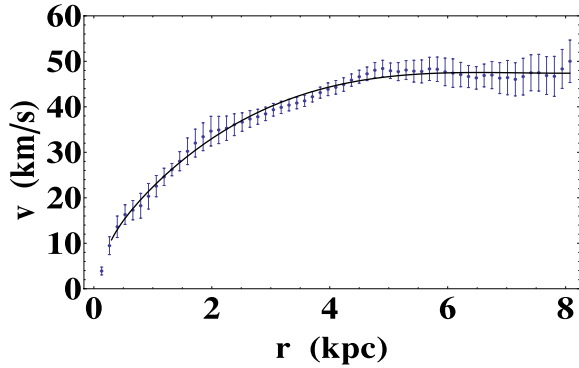


**Figure 24.** Eight-parameter series fit of rotation velocity data for DD0 154 from  $r = 0.3$  to 8 kpc.

(A color version of this figure is available in the online journal.)

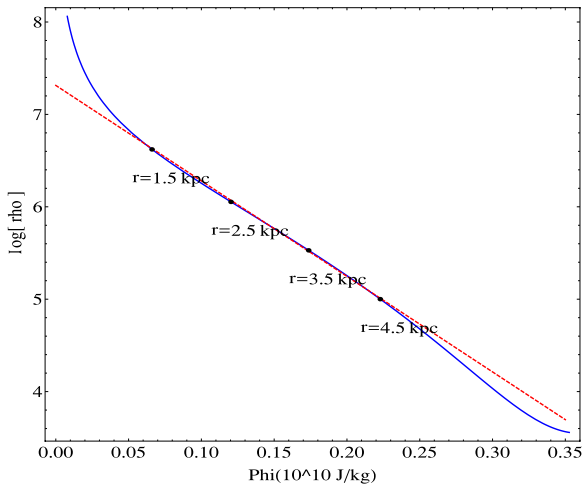


**Figure 25.**  $\log(\text{density}/\text{constant})$  vs. the gravitational potential for DD0 154 for  $r = 0.3$  to 8 kpc. It is compared to a straight line (red, dashed) with slope  $\approx -8600 \text{ eV K}^{-1}$ . The two plots approximately coincide for  $1.5 < r < 4.5$  kpc.

(A color version of this figure is available in the online journal.)

Figure 26, we plot minus the derivative of  $\log \rho$  with  $\phi$  versus  $r$ . It ranges between  $\sim 7500 \text{ eV K}^{-1}$  and  $\sim 10,000 \text{ eV K}^{-1}$  and has an average value of  $\sim 8600 \text{ eV K}^{-1}$  for the domain  $1.5 < r < 6.5$  kpc.

### 3. AN EFFECTIVE THEORY

In the previous section, we presented evidence of Boltzmann-like behavior in regions of halos of eight galaxies in the THINGS survey. Here we model the Boltzmann behavior by writing down the dynamics for a self-gravitating gas in the thermodynamic equilibrium in an external gravitational field. The relevant domain for the model is a finite shell, associated with the regions where the exponential behavior was found for  $\rho$  versus  $\phi$ . Here we discuss the parameter space of the solutions of the model, along with consistency checks. Fits of the rotation curves to the solutions will be made in the following section.

#### 3.1. Dynamics and Boundary Conditions

Here we write down an effective thermodynamic model for regions, corresponding to spherical shells  $R_G \leq r \leq R_{\max}$ , where the Boltzmann gas is valid. More specifically, it is the description of a self-gravitating isothermal gas, subject to an external gravitational potential. The total gravitational potential is again denoted by  $\phi$ , which includes contributions from the

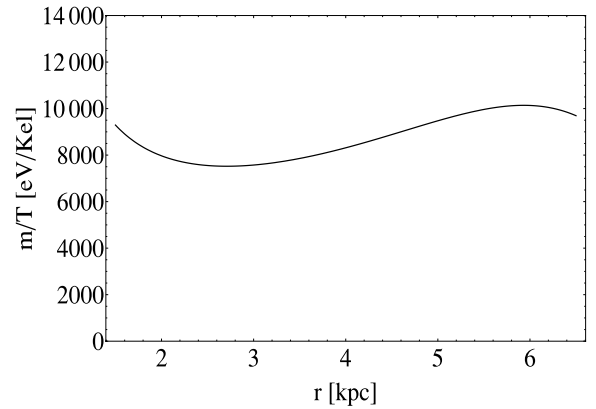


**Figure 26.**  $-(d \log \rho / d \phi)$  vs.  $r$  for DD0 154. The plot ranges between  $\sim 7500 \text{ eV K}^{-1}$  and  $\sim 10,000 \text{ eV K}^{-1}$  over the domain  $1.5 < r < 6.5$  kpc.

gravitational self-interactions of the gas, as well as the external tidal force. We shall assume that the gas consists of only one type of particle, with mass  $m$ , and that  $\phi$  is slowly varying with respect to the average interparticle distance. As in the previous section, we assume that spherical symmetry holds, at least at lowest order, and so quantities of interest, such as  $\phi$  and the average density  $\rho$  are functions only of the radial variable. It is desirable to have the radius  $R_G$  of the inner boundary sufficiently larger than the distance scale of the disk. (This was generally the case for the examples considered in the previous section. For instance,  $R_G$  was approximately twice the disk scale for NGC 2841.) Then one expects that deviations from spherical symmetry and contributions from the baryonic matter to total density  $\rho$  in the spherical shell can be ignored at lowest order.

We first impose boundary conditions at  $r = R_G$ . The value of  $\phi$  at the boundary is arbitrary. It is convenient to choose it to be zero.<sup>4</sup> Then for a Boltzmann gas one has

$$\rho(r) = \rho(R_G) e^{-m\phi(r)/k_B T}. \quad (3)$$

On the other hand, the value of  $(d\phi/dr)$  at  $r = R_G$  must be identified with the acceleration of gravity at the inner boundary of the spherical shell. Thus

$$\phi(R_G) = 0 \quad \left. \frac{d\phi}{dr} \right|_{r=R_G} = \frac{GM_G}{R_G^2}, \quad (4)$$

$M_G$  is the total mass inside the sphere of radius  $R_G$ . The model is thus defined by the two boundary conditions and the Poisson equation

$$\frac{1}{r^2} \frac{d}{dr} \left( r^2 \frac{d\phi}{dr} \right) = 4\pi G \rho(R_G) e^{-m\phi(r)/k_B T}, \quad R_G \leq r \leq R_{\max}. \quad (5)$$

The pressure balance implicitly holds everywhere within and beyond the isothermal region, including at the interfaces between the regions. The pressure within the isothermal region is given by the ideal gas equation  $P(r) = \rho(r)kT/m$ .

#### 3.2. Solutions

To examine the space of solutions, it is convenient to do a rescaling to the dimensionless variables  $x = (r/R_G)$  and

<sup>4</sup> Our fitting procedure will not depend on this choice. The fits determine values of  $\rho(R_G)$  and  $m/T$  in the density formula (3). The addition of a constant to the potential can be absorbed in  $\rho(R_G)$ .

$\chi = (R_G/GM_G)\phi$ . Equation (5) simplifies to

$$\frac{1}{x^2} \frac{d}{dx} \left( x^2 \frac{d\chi}{dx} \right) = 3\kappa e^{-\frac{\chi(x)}{\tau}}, \quad 1 \leq x \leq x_{\max}, \quad (6)$$

where  $x_{\max} = R_{\max}/R_G$ , and the boundary conditions become

$$\chi(1) = 0 \quad \left. \frac{d\chi}{dx} \right|_{x=1} = 1. \quad (7)$$

$\kappa$  and  $\tau$  are independent dimensionless parameters determining the solutions. They depend, among other things, on  $R_G$  and  $M_G$ .  $\kappa$  is the ratio of  $\rho(R_G)$  to the mean mass density in the interior of the sphere of radius  $R_G$ , i.e.,  $\rho_G = M_G/((4/3)\pi R_G^3)$ , while  $\tau$  is a rescaled temperature

$$\kappa = \frac{4\pi R_G^3 \rho(R_G)}{M_G} \quad \tau = \frac{k_B T}{m v_{x=1}^2}, \quad (8)$$

where  $v_{x=1}$  is the speed of objects undergoing circular orbits at  $r = R_G$ . It is given by  $v_{x=1}^2 = GM_G/R_G$ . From solutions to Equations (6) and (7), one can then determine the orbital speed  $v(x)$  at any value of the radial coordinate, along with the total mass  $M(x)$  enclosed in a sphere of radius  $x$ ,  $1 \leq x \leq x_{\max}$ . They are given, respectively, by

$$\left( \frac{v}{v_{x=1}} \right)^2 = x \frac{d\chi}{dx} \quad \text{and} \quad \frac{M(x)}{M_G} = 3\kappa \int_1^x dx' x'^2 e^{-\frac{\chi(x')}{\tau}}. \quad (9)$$

Equation (6) is the spherically symmetric Lane-Emden equation for an infinite polytropic index, which is often referred to as the Emden equation (Emden 1907). Various techniques have been employed to obtain its solutions, and application to galactic dynamics has been discussed. (See, e.g., Peebles 1993; Liu 1996; Natarajan & Lynden-Bell 1997; Mishchenko & Ji 2003. Axially symmetric solutions with rotation have also been obtained; Christodoulou & Kazanas 2007.) Boundary conditions for this equation are standardly imposed at the origin, where the gravitational force is required to vanish, i.e.,  $d\chi/dx|_{x=0} = 0$ .<sup>5</sup> This boundary condition leads to a solution known as the isothermal sphere, which was first found by Emden.

In our case, the Boltzmann gas description is not valid outside the domain  $1 \leq x \leq x_{\max}$ , and it is then appropriate to impose boundary conditions at  $x = 1$ , as we have done in Equation (7). A two-parameter (i.e.,  $\kappa$  and  $\tau$ ) family of solutions to the Emden equations result from the boundary conditions (7).

The solutions contain Emden's isothermal sphere as a special case. That is, a subset of the solutions to Equations (6) and (7) can be consistently continued from  $x = 1$  to the origin, where  $d\chi/dx|_{x=0} = 0$ .  $\kappa$  and  $\tau$  are not independent for the subset. To see this, one can do another rescaling of the field,  $\chi \rightarrow \tilde{\chi} = \chi/\tau$ , and the coordinate,  $x \rightarrow \tilde{x} = \sqrt{(3\kappa/\tau)}x$ , thereby removing the parameters from the differential Equation (6), and putting them instead in the boundary conditions. Then

$$\frac{1}{\tilde{x}^2} \frac{d}{d\tilde{x}} \left( \tilde{x}^2 \frac{d\tilde{\chi}}{d\tilde{x}} \right) = e^{-\tilde{\chi}(\tilde{x})}, \quad (10)$$

with

$$\tilde{\chi} \Big|_{\tilde{x}=\sqrt{\frac{3\kappa}{\tau}}} = 0 \quad \left. \frac{d\tilde{\chi}}{d\tilde{x}} \right|_{\tilde{x}=\sqrt{\frac{3\kappa}{\tau}}} = \frac{1}{\sqrt{3\kappa\tau}}. \quad (11)$$

<sup>5</sup>  $\chi$  is often set to zero, as well, at the origin, but this is a gauge condition which can be removed with a redefinition of  $\kappa$ .

For generic values of  $\kappa$  and  $\tau$ , the boundary conditions (11) cannot be generated by integrating the Emden equation from the origin, starting from  $d\tilde{\chi}/d\tilde{x}|_{\tilde{x}=0} = 0$  and any  $\tilde{\chi}(0)$ . [ $\tilde{\chi}(0)$  must be negative since  $\tilde{\chi}$  grows with increasing  $\tilde{x}$ .] If one were to impose the boundary condition  $d\tilde{\chi}/d\tilde{x}|_{\tilde{x}=0} = 0$ , along with some  $\tilde{\chi}(0) < 0$ , one can integrate the Emden equations to find the intersection of  $\tilde{\chi}(\tilde{x})$  with the  $\tilde{x}$ -axis, along with the slope of the function at that point. The result, along with Equation (11), can then be used to numerically solve for specific values of  $\kappa$  and  $\tau$ , associated with the subset of isothermal spheres.

Another special solution to the Emden equation is the ‘‘singular’’ isothermal sphere. It has the analytic expression

$$\chi(x) = \tau \log \left( \frac{3\kappa x^2}{2\tau} \right). \quad (12)$$

It is called singular because it is ill-defined at the origin (for any values of  $\kappa$  and  $\tau$ ). Rather than satisfying  $d\chi/dx|_{x=0} = 0$ , the acceleration of gravity diverges at the origin. On the other hand, Equation (12) is mathematically and physically well defined for the domain of interest here,  $1 \leq x \leq x_{\max}$ . It satisfies the boundary conditions (7) for particular values of  $\tau$  and  $\kappa$ , namely,  $\tau = 1/2$  and  $\kappa = 1/3$ , or in terms of dimensionfull quantities,

$$\rho(R_G) = \frac{M_G}{4\pi R_G^3} \quad \frac{m}{T} = \frac{2k_B}{v_{x=1}^2}. \quad (13)$$

From  $v_{x=1}^2 = GM_G/R_G$ , one finds that  $m/T$  in (13) is determined by the baryonic matter and dark matter contained in  $r < R_G$ . Using Equation (9), we find that the solution (12) gives exactly flat rotation curves,  $v = v_{x=1}$  for all  $x > 0$ , and the linear mass function  $M(x) = (x - 1)M_G$ . Since this behavior is roughly what is observed for all galactic halos, Equation (13) should provide crude estimates for  $\rho(R_G)$  and  $m/T$ . In Section 4, we shall compare these estimates to values extracted from fits to the rotation curve data, and we can compare the fitted values of  $\kappa$  and  $\tau$  to this special case.

Although Equation (12) is not a solution for arbitrary values of  $\tau$  and  $\kappa$ , it does describe the behavior of generic solutions as  $x \rightarrow \infty$ .<sup>6</sup> So in the asymptotic region of the solution (which may be beyond the relevant physical domain,  $1 \leq x \leq x_{\max}$ ), the orbital speed goes to a constant value, specifically,

$$v_\infty = \sqrt{2\tau} v_{x=1} = \sqrt{\frac{2k_B T}{m}}, \quad (14)$$

for any  $\kappa > 0$ . (Of course,  $v \rightarrow 0$  as  $x \rightarrow \infty$  in the absence of any matter source in the region, i.e.,  $\kappa = 0$ .) This is illustrated in Figures 27 and 28. There we plot  $v/v_{x=1}$  for numerical solutions to Equations (6) and (7) associated with using various values of  $\tau$  and  $\kappa$  (including the values  $\tau = 1/2$  and  $\kappa = 1/3$  associated with the analytic solution (12)).

### 3.3. Consistency Checks

Since we are dealing with a Boltzmann gas description, it is reasonable to regard the effective temperature as a measure of the average kinetic energy of the dark matter particles. Then a simple

<sup>6</sup> To see this, we can do another change of coordinates and rewrite the differential equation in terms of  $y = \log x$ . Upon assuming that  $(d^2\chi/dy^2) \ll (d\chi/dy)$  when  $y \rightarrow \infty$ , one gets  $(d\chi/dy) \sim 3\kappa \exp(2y - \chi(y)/\tau)$ , the solution of which is Equation (12).

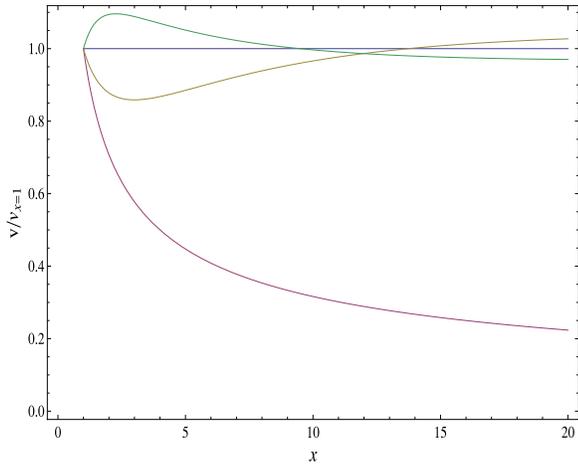


**Figure 27.**  $v/v_{x=1}$  is plotted vs.  $x$  for  $\tau = 1/2$  and  $\kappa = 0, 1/6, 1/3,$  and  $1/2$ . The values of  $\kappa$  are listed in ascending order of the slope at  $x = 1$ , with  $\kappa = 0$  corresponding to no halo.

(A color version of this figure is available in the online journal.)

application of the equipartition theorem gives an rms speed of  $u = \sqrt{3k_B T/m}$ , assuming no internal structure for the particles. This is of the same order as the average orbital speed of the H I gas in the halo. From Equation (14), one gets  $u = \sqrt{(3/2)}v_\infty$ , where  $v_\infty$  was the orbital speed in the limit  $r$  tends to infinity. Since orbital speeds in halos are nonrelativistic, the particles in this Boltzmann gas description must also be nonrelativistic. This provides one consistency check of the model as no relativistic corrections need to be considered.

Another consistency check comes from examining the number density  $n(r) = \rho(r)/m$ . A Boltzmann gas description necessitates that the particles behave classically. This means that the de Broglie wavelength  $\lambda$  is much less than the interparticle distance,

$$\lambda n^{1/3}(r) \ll 1. \quad (15)$$

As our analysis applies only for the domain  $R_G \leq r \leq R_{\max}$ , the most stringent constraint will be at the inner boundary of the shell,  $r = R_G$ . Applying this to the example of the solution with  $\tau = 1/2$  and  $\kappa = 1/3$ , which is associated with exactly flat rotation curves, one has from Equation (13) that  $n(R_G) = M_G/(4\pi m R_G^3)$ , while  $\lambda = (h/mu) = \sqrt{(2/3)}(h/mv_\infty)$ . The condition (15) becomes

$$m^{8/3} \gg \frac{8\pi}{3^{5/3}} \left( \frac{\hbar \rho_G^{1/3}}{v_\infty} \right)^2, \quad (16)$$

where  $\rho_G$  is again the mean mass density inside the sphere of radius  $R_G$ . For an order of magnitude estimate, let us take  $\rho_G \sim 10^9 M_\odot \text{ kpc}^{-3}$  along with  $v_\infty \sim 200 \text{ km s}^{-1}$ . Substituting into the right hand side of Equation (16) gives  $\sim (100 \text{ eV})^{8/3}$ . Thus, the classical approximation is valid provided that particle mass is significantly greater than  $\sim 100 \text{ eV}$ . In other words, corrections due to quantum statistics can only be significant in the spherical shell,  $R_G \leq r \leq R_{\max}$ , if the dark matter particle mass is  $\sim 100 \text{ eV}$  or less (smaller bounds result from typical densities of dwarf galaxies). However, since such hot dark matter scenarios are currently disfavored, classical statistics is all that is needed for this model.

#### 4. BOLTZMANN FITS

In Section 2 we fit the rotation velocity data for galactic halos to an eight-parameter series and found significant regions

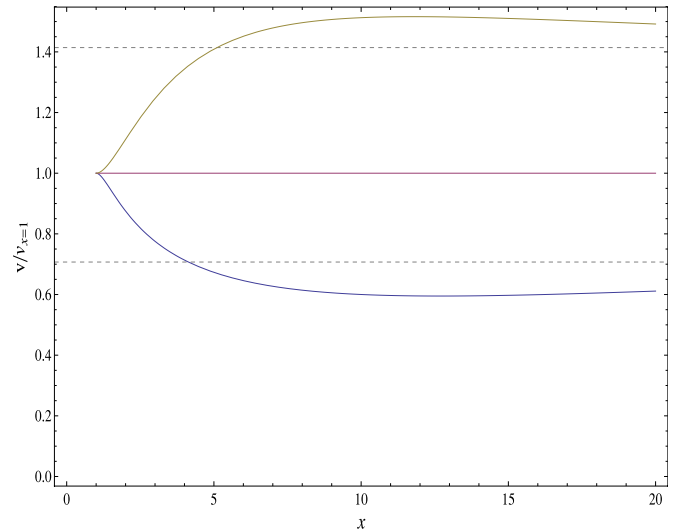


**Figure 28.**  $v/v_{x=1}$  is plotted vs.  $x$  for  $\kappa = 1/3$  and  $\tau = 1/4, 1/2,$  and  $1$ . The values of  $\tau$  are listed in ascending order of the slope at  $x = 1$ . The limiting value of  $v/v_{x=1}$  is  $\sqrt{2}\tau$ , which is indicated for the top and bottom curves by the dashed gridlines.

(A color version of this figure is available in the online journal.)

$R_G \leq r \leq R_{\max}$  in the halos where  $\rho(\phi)$  decreases exponentially. Here we directly compare the data in this region to the model of the self-gravitating isothermal Boltzmann gas constructed in the previous section. More specifically, we fit the rotational velocity data from THINGS (de Blok et al. 2008) to solutions of Equations (4) and (5). As stated in the introduction, our procedure is very different from the common practice of fitting the data using some particular density profile for the dark matter, such as NFW. The latter requires detailed knowledge of all the baryonic contributions, which are deduced from mass models. The results of such fits are highly dependent on the choice of mass models. On the other hand, precise density profiles for the baryonic contributions are not required in the analysis we do here. The baryonic component, nevertheless, plays an important role in our approach. It, along with the dark matter contribution to the mass  $M(R_G)$  in the interior region  $r \leq R_G$ , determine the second boundary condition in Equation (4) at  $R_G$ , which gives the strength of the external gravitational field in the spherical shell  $R_G \leq r \leq R_{\max}$ . (In practice, we do the inverse. We determine the boundary condition from the fits, i.e., we obtain  $M(R_G)$  from the data.) As the purpose of this section is to test the validity of the model, it makes sense to restrict the fit to the region  $R_G \leq r \leq R_{\max}$ , where the Boltzmann-like behavior was previously found.

The Boltzmann fits allow us to determine the three dimension-full parameters of the model, namely,  $m/T$ ,  $\rho(R_G)$ , and  $M(R_G)$ , for the given  $R_G$ . From them, we do the following:

1. We compare the results for  $m/T$  to those found in Section 2.
2. Using the Boltzmann form for the density (3), we numerically estimate the mass  $M_{(R_G, R_{\max})}$  of the region,  $R_G \leq r \leq R_{\max}$ . The mass of the Boltzmann-like region is simply

$$M_{(R_G, R_{\max})} = 4\pi \rho(R_G) \int_{R_G}^{R_{\max}} dr r^2 e^{-m\phi(r)/k_B T}. \quad (17)$$

In order to understand what fraction of the total mass of the galaxy it represents, we compare  $M_{(R_G, R_{\max})}$  to the mass  $M(R_G)$  in the interior region  $r < R_G$ , and to the total

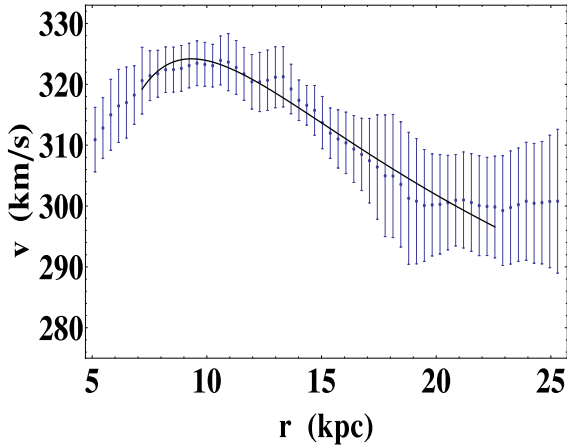


**Figure 29.** Fit of the rotation velocity data for NGC 2841 to a Boltzmann gas in the region  $7 \text{ kpc} \leq r \leq 22 \text{ kpc}$ . The fitted value for the three dimensionfull parameters of the Boltzmann gas are  $m/T \approx 205 \text{ eV K}^{-1}$ ,  $\rho(R_G) \approx 4.6 \times 10^7 M_\odot \text{ kpc}^{-3}$ , and  $M(R_G) \approx 1.7 \times 10^{11} M_\odot$ . (A color version of this figure is available in the online journal.)

baryonic mass of the galaxy, as was determined previously from a mass model (de Blok et al. 2008).

3. Lastly, we obtain fitted values for the dimensionless parameters  $\kappa$  and  $\tau$  and compare the results to the flat solution  $(\tau, \kappa) = (1/2, 1/3)$ .

We again consider the eight galaxies in the order: unbarred, weakly barred, barred, and dwarf galaxies.

#### 4.1. NGC 2841

In Section 2.1 the exponential behavior for  $\rho(\phi)$  was found in the region  $7 \text{ kpc} \leq r \leq 22 \text{ kpc}$  of the NGC 2841 halo. Here we perform the fit in this region of the rotation velocity data to solutions of Equations (4) and (5). It is shown in Figure 29. The fit is done to the midpoints (corresponding to the dots) of the error bars. The values found for the three dimensionfull parameters of the Boltzmann gas are  $m/T \approx 205 \text{ eV K}^{-1}$ ,  $\rho(R_G) \approx 4.6 \times 10^7 M_\odot \text{ kpc}^{-3}$ , and  $M(R_G) \approx 1.7 \times 10^{11} M_\odot$ . The result for  $m/T$  is close to the value of  $\sim 190 \text{ eV K}^{-1}$  obtained in Section 2. The latter corresponds to the average of  $-(d \log \rho / d\phi)$  over the domain  $7 < r < 22 \text{ kpc}$  in Figure 5. One can also compare the results for  $\rho(R_G)$  and  $M(R_G)$  with those of the eight-parameter fit in Section 2. For  $\rho(7 \text{ kpc})$ , the latter gives  $\sim 4.4 \times 10^7 M_\odot \text{ kpc}^{-3}$  which is close to the result obtained from the Boltzmann fit. More generally, to calculate  $M(R_G)$  from the eight-parameter fit, one can use  $M(R_G) = v(R_G)^2 R_G / G$ . The result is  $M(7 \text{ kpc}) \sim 1.67 \times 10^{11} M_\odot$ . This value is also close to the result we get for the Boltzmann fit. In Figure 30, we plot the Boltzmann gas density for the fitted values of the parameters and compare it with the density in Figure 3, which was obtained from the eight-parameter series fit. Agreement is quite close beyond 10 kpc. (The analogous comparisons for the other seven galaxies [not shown here] are reasonably similar, with one exception.)

We next numerically estimate the mass of the Boltzmann-like region  $7 < r < 22 \text{ kpc}$  using Equation (17). We get  $M_{(7 \text{ kpc}, 22 \text{ kpc})} \approx 2.9 \times 10^{11} M_\odot$ . It is significantly greater than the mass  $M(R_G)$  of the inner region,  $r < 7 \text{ kpc}$ . Furthermore, it is also significantly greater than the sum of the baryonic mass contributions for NGC 2841, which were obtained from a mass model (de Blok et al. 2008). Summing the disk, bulge,

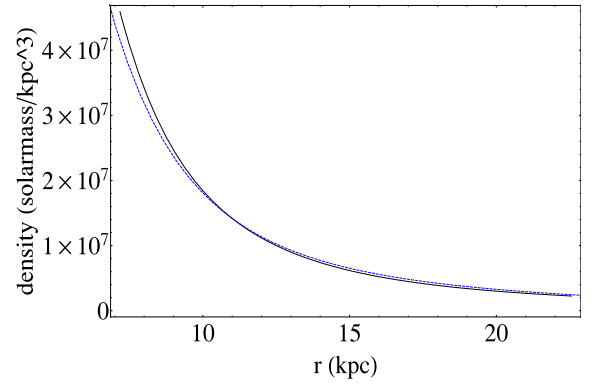


**Figure 30.** Plot of the Boltzmann gas density for the fitted values of the parameters (solid) compared to the density resulting from the eight-parameter series fit in Section 2 which was obtained from the eight-parameter series fit restricted to the region  $7 \text{ kpc} \leq r \leq 22 \text{ kpc}$  (dashed).

(A color version of this figure is available in the online journal.)

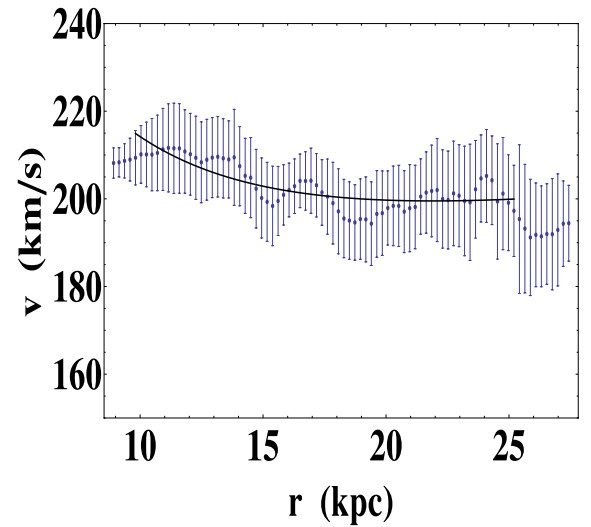


**Figure 31.** Fit of the rotation velocity data for NGC 5055 to a Boltzmann gas in the region  $10 \text{ kpc} \leq r \leq 25 \text{ kpc}$ . The fitted values for the three dimensionfull parameters of the Boltzmann gas are  $m/T \approx 300 \text{ eV K}^{-1}$ ,  $\rho(R_G) \approx 5.7 \times 10^6 M_\odot \text{ kpc}^{-3}$ , and  $M(R_G) \approx 1.05 \times 10^{11} M_\odot$ .

(A color version of this figure is available in the online journal.)

and HI gas masses cited in Section 2.1 gives  $\sim 1.43 \times 10^{11} M_\odot$  (which in this example is close to the estimate for the mass  $M(R_G)$  in the inner region). From these values, one gets that the region exhibiting Boltzmann-like behavior is more than twice as massive as the baryonic component of the galaxy, and it therefore must consist mainly of dark matter.

From Equation (8), we compute the fitted values for the dimensionless parameters  $\tau$  and  $\kappa$ . We get  $\tau \approx 0.37$  and  $\kappa \approx 0.42$ . This in contrast to the trivial isothermal solution  $(\tau, \kappa) = (1/2, 1/3)$ , associated with an exactly flat rotation curve. Since  $v(r)$  is far from being flat, it is a non-trivial result that the region  $7 < r < 22 \text{ kpc}$  is well described by a Boltzmann gas.

#### 4.2. NGC 5055

In Section 2.2, the exponential behavior for  $\rho(\phi)$  was found in the region  $10 < r < 25 \text{ kpc}$  of the NGC 5055 halo. A fit in this region of the rotation velocity data to the solutions of Equations (4) and (5) is shown in Figure 31. The fitted value

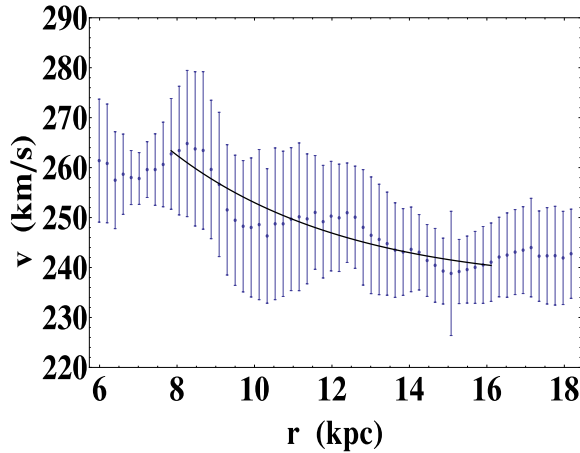


**Figure 32.** Fit of the rotation velocity data for NGC 7331 to a Boltzmann gas in the region  $8 \text{ kpc} \leq r \leq 16 \text{ kpc}$ . The fitted values for the three dimensionfull parameters of the Boltzmann gas are  $m/T \approx 225 \text{ eV K}^{-1}$ ,  $\rho(R_G) \approx 1.3 \times 10^7 M_\odot \text{ kpc}^{-3}$ , and  $M(R_G) \approx 1.3 \times 10^{11} M_\odot$ . (A color version of this figure is available in the online journal.)

for the three dimensionfull parameters of the Boltzmann fit are  $m/T \approx 300 \text{ eV K}^{-1}$ ,  $\rho(R_G) \approx 5.7 \times 10^6 M_\odot \text{ kpc}^{-3}$ , and  $M(R_G) \approx 1.05 \times 10^{11} M_\odot$ . The fit for  $m/T$  is a bit below the average value of  $\sim 440 \text{ eV K}^{-1}$  found for this region from Figure 8, but is somewhat sensitive to the choice of end points. Using Equation (17), we can numerically estimate the mass of the region  $10 < r < 25 \text{ kpc}$  exhibiting Boltzmann-like behavior. We get  $M_{(10 \text{ kpc}, 25 \text{ kpc})} \approx 1.29 \times 10^{11} M_\odot$ . This is approximately the same as the estimated value of the mass  $M(R_G)$  in the interior region  $r < R_G$ , and it is also approximately the same as the sum of the baryonic mass contributions for NGC 5055 quoted in Section 2.2. The latter is  $\sim 1.34 \times 10^{11} M_\odot$ . From Equation (8) the fitted values for  $\tau$  and  $\kappa$  are  $\tau \approx 0.55$  and  $\kappa \approx 0.21$ , as compared with the flat solution  $(\tau, \kappa) = (1/2, 1/3)$ .

#### 4.3. NGC 7331

In Section 2.3, the exponential behavior for  $\rho(\phi)$  was found in the region  $8 < r < 16 \text{ kpc}$  of the NGC 7331 halo. A fit in this region of the rotation velocity data to the solutions of Equations (4) and (5) is shown in Figure 32. The fitted value for the three dimensionfull parameters of the Boltzmann fit are  $m/T \approx 225 \text{ eV K}^{-1}$ ,  $\rho(R_G) \approx 1.3 \times 10^7 M_\odot \text{ kpc}^{-3}$ , and  $M(R_G) \approx 1.3 \times 10^{11} M_\odot$ . The fit for  $m/T$  is to be compared to the average value of  $\sim 260 \text{ eV K}^{-1}$  found for this region from Figure 10. Using Equation (17), we can numerically estimate the mass of the region  $8 < r < 16 \text{ kpc}$ . We get  $M_{(8 \text{ kpc}, 16 \text{ kpc})} \approx 0.90 \times 10^{11} M_\odot$ , which is a little less than the mass  $M(R_G)$  in the interior region  $r < R_G$ . The sum of the quoted baryonic mass contributions for NGC 7331 in Section 2.3, which were obtained from a mass model is  $\sim 1.925 \times 10^{11} M_\odot$  (de Blok et al. 2008). From (8) the fitted values for  $\tau$  and  $\kappa$  are  $\tau \approx 0.50$  and  $\kappa \approx 0.21$ .

#### 4.4. NGC 2403

In Section 2.4, we found exponential behavior for  $\rho(\phi)$  in the region  $3 < r < 10 \text{ kpc}$  of the halo for weakly barred spiral galaxy NGC 2403. A fit of the rotation velocity data to the solutions of Equations (4) and (5) in the region is shown in Figure 33. The fitted value for the three dimensionfull parameters of the Boltzmann fit are  $m/T \approx 1140 \text{ eV K}^{-1}$ ,  $\rho(R_G) \approx 3.5 \times 10^7 M_\odot \text{ kpc}^{-3}$ , and  $M(R_G) \approx 5.9 \times 10^9 M_\odot$ .

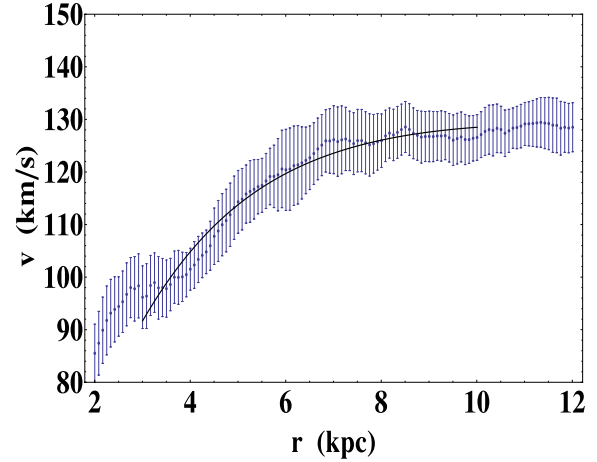


**Figure 33.** Fit of the rotation velocity data for NGC 2403 to a Boltzmann gas in the region  $3 \text{ kpc} \leq r \leq 10 \text{ kpc}$ . The fitted values for the three dimensionfull parameters of the Boltzmann gas are  $m/T \approx 1140 \text{ eV K}^{-1}$ ,  $\rho(R_G) \approx 3.5 \times 10^7 M_\odot \text{ kpc}^{-3}$ , and  $M(R_G) \approx 5.9 \times 10^9 M_\odot$ . (A color version of this figure is available in the online journal.)

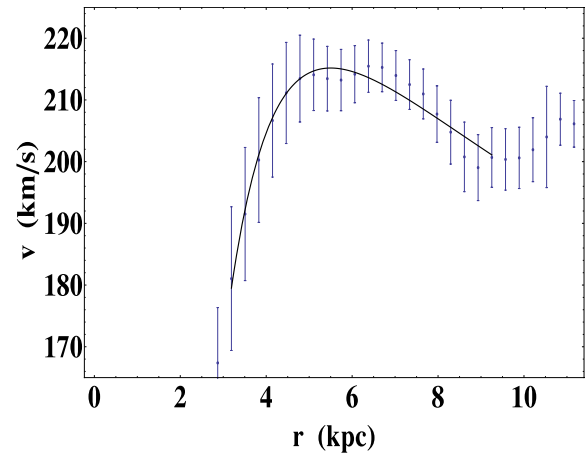


**Figure 34.** Fit of the rotation velocity data for NGC 2903 to a Boltzmann gas in the region  $3 \text{ kpc} \leq r \leq 9 \text{ kpc}$ . The fitted values for the three dimensionfull parameters of the Boltzmann gas are  $m/T \approx 580 \text{ eV K}^{-1}$ ,  $\rho(R_G) \approx 1.6 \times 10^8 M_\odot \text{ kpc}^{-3}$ , and  $M(R_G) \approx 2.4 \times 10^{10} M_\odot$ . (A color version of this figure is available in the online journal.)

The fit for  $m/T$  is close to the average value of  $\sim 1100 \text{ eV K}^{-1}$ , found for this region from Figure 13. Using Equation (17), we can numerically estimate the mass of the region  $3 < r < 10 \text{ kpc}$ . We get  $M_{(3 \text{ kpc}, 10 \text{ kpc})} \approx 3.25 \times 10^{10} M_\odot$ , which is over five times the mass  $M(R_G)$  in the interior region  $r < R_G$ . It is also much greater than the combined baryonic mass contributions from a mass model for NGC 2403, as was cited in Section 2.4. The latter is  $\sim 7.7 \times 10^9 M_\odot$ . From Equation (8), the fitted values for  $\tau$  and  $\kappa$  are  $\tau \approx 0.81$  and  $\kappa \approx 0.67$ .

#### 4.5. NGC 2903

A fit of the rotation velocity data to the solutions of Equations (4) and (5) in the region  $3 < r < 9 \text{ kpc}$  is shown in Figure 34. The fitted value for the three dimensionfull parameters of the Boltzmann fit are  $m/T \approx 580 \text{ eV K}^{-1}$ ,  $\rho(R_G) \approx 1.6 \times 10^8 M_\odot \text{ kpc}^{-3}$ , and  $M(R_G) \approx 2.4 \times 10^{10} M_\odot$ . The result for  $m/T$  is compared with the average value of  $\sim 490 \text{ eV K}^{-1}$  found in Figure 16. Using Equation (17), we can numerically estimate the mass of the region  $3 < r < 9 \text{ kpc}$ . We get  $M_{(3 \text{ kpc}, 9 \text{ kpc})} \approx 6.3 \times 10^{10} M_\odot$ . This is significantly greater

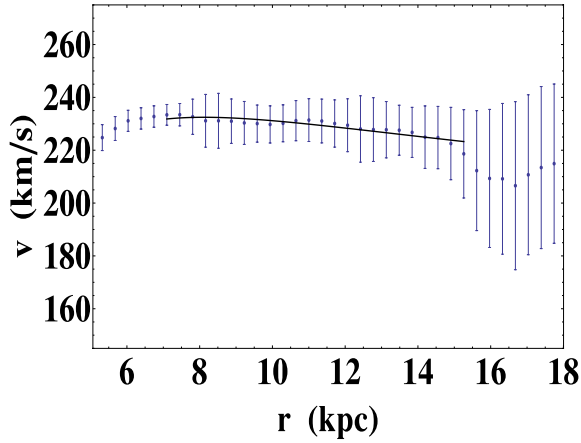


**Figure 35.** Fit of the rotation velocity data for NGC 3521 to a Boltzmann gas in the region  $7 \text{ kpc} \leq r \leq 15 \text{ kpc}$ . The fitted values for the three dimensionfull parameters of the Boltzmann gas are  $m/T \approx 370 \text{ eV K}^{-1}$ ,  $\rho(R_G) \approx 2.1 \times 10^7 M_\odot \text{ kpc}^{-3}$ , and  $M(R_G) \approx 8.9 \times 10^{10} M_\odot$ .

(A color version of this figure is available in the online journal.)

than the mass  $M(R_G)$  in the interior region  $r < R_G$  and also the combined baryonic mass contributions from a mass model for NGC 2903. Using the values quoted in Section 2.5, the latter is  $\sim 2.06 \times 10^{10} M_\odot$ . From Equation (8), the fitted values for  $\tau$  and  $\kappa$  are  $\tau \approx 0.41$  and  $\kappa \approx 0.90$ .

#### 4.6. NGC 3521

A fit of the rotation velocity data to the solutions of Equations (4) and (5) in the region  $7 < r < 15 \text{ kpc}$  is shown in Figure 35. The fitted value for the three dimensionfull parameters of the Boltzmann fit are  $m/T \approx 370 \text{ eV K}^{-1}$ ,  $\rho(R_G) \approx 2.1 \times 10^7 M_\odot \text{ kpc}^{-3}$ , and  $M(R_G) \approx 8.9 \times 10^{10} M_\odot$ . The fit for  $m/T$  is close to the average value of  $380 \text{ eV K}^{-1}$ , found for this region in Figure 19. Using Equation (17), we can numerically estimate the mass of the region  $7 < r < 15 \text{ kpc}$ . We get  $M_{(7 \text{ kpc}, 15 \text{ kpc})} \approx 8.8 \times 10^{10} M_\odot$ , which is approximately the same as the mass  $M(R_G)$  in the interior region  $r < R_G$ . This is compared with the sum of the quoted baryonic mass contributions in Section 2.6 for NGC 3521 of  $\sim 1.31 \times 10^{11} M_\odot$ . From Equation (8) the fitted values for  $\tau$  and  $\kappa$  are  $\tau \approx 0.39$  and  $\kappa \approx 0.36$ .

#### 4.7. NGC 3198

For the case of the barred spiral galaxy NGC 3198, a fit of the rotation velocity data to the solutions of Equations (4) and (5) in the region  $5 < r < 20 \text{ kpc}$  is shown in Figure 36. The fitted value for the three dimensionfull parameters of the Boltzmann fit are  $m/T \approx 800 \text{ eV K}^{-1}$ ,  $\rho(R_G) \approx 2.2 \times 10^7 M_\odot \text{ kpc}^{-3}$ , and  $M(R_G) \approx 1.9 \times 10^{10} M_\odot$ . The fit for  $m/T$  is within the range of values for this region found from Figure 23. Using Equation (17), we can numerically estimate the mass of the region  $5 < r < 20 \text{ kpc}$ . We get  $M_{(5 \text{ kpc}, 20 \text{ kpc})} \approx 8.9 \times 10^{10} M_\odot$ , which is much greater than the mass  $M(R_G)$  in the interior region  $r < R_G$ . It is also greater than the sum of the stated baryonic masses for NGC 3198 in Section 2.7. The latter is  $4.12 \times 10^{10} M_\odot$ . From (8), the fitted values for  $\tau$  and  $\kappa$  are  $\tau \approx 0.58$  and  $\kappa \approx 0.59$ .

#### 4.8. DD0 154

Lastly, for the case of the dwarf galaxy DD0 154, a fit of the rotation velocity data to the solutions of Equations (4) and (5) in

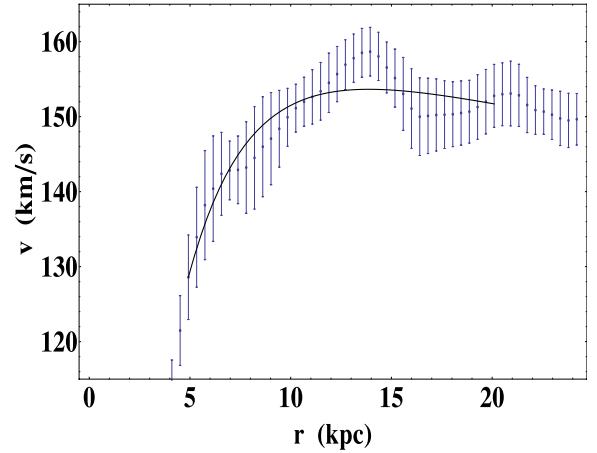


**Figure 36.** Fit of the rotation velocity data for NGC 3198 to a Boltzmann gas in the region  $5 \text{ kpc} \leq r \leq 20 \text{ kpc}$ . The fitted values for the three dimensionfull parameters of the Boltzmann gas are  $m/T \approx 800 \text{ eV K}^{-1}$ ,  $\rho(R_G) \approx 2.2 \times 10^7 M_\odot \text{ kpc}^{-3}$ , and  $M(R_G) \approx 1.9 \times 10^{10} M_\odot$ .

(A color version of this figure is available in the online journal.)

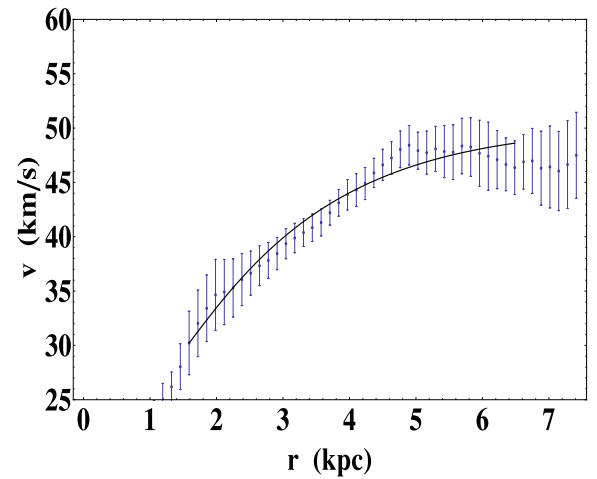


**Figure 37.** Fit of the rotation velocity data for DD0 154 to a Boltzmann gas in the region  $1.5 \text{ kpc} \leq r \leq 6.5 \text{ kpc}$ . The fitted values for the three dimensionfull parameters of the Boltzmann gas are  $m/T \approx 7500 \text{ eV K}^{-1}$ ,  $\rho(R_G) \approx 1.2 \times 10^7 M_\odot \text{ kpc}^{-3}$ , and  $M(R_G) \approx 3.4 \times 10^8 M_\odot$ .

(A color version of this figure is available in the online journal.)

the region  $1.5 < r < 6.5 \text{ kpc}$  is shown in Figure 37. The fitted value for the three dimensionfull parameters of the Boltzmann fit are  $m/T \approx 7500 \text{ eV K}^{-1}$ ,  $\rho(R_G) \approx 1.2 \times 10^7 M_\odot \text{ kpc}^{-3}$ , and  $M(R_G) \approx 3.4 \times 10^8 M_\odot$ . The fit for  $m/T$  is within the range found for this region from Figure 26. Using Equation (17), we can numerically estimate the mass of the region  $1.5 < r < 6.5 \text{ kpc}$ . We get  $M_{(1.5 \text{ kpc}, 6.5 \text{ kpc})} \approx 3.2 \times 10^9 M_\odot$ , which is an order of magnitude bigger than the mass  $M(R_G)$  in the interior region  $r < R_G$ . It is also approximately an order of magnitude bigger than the sum of the stated baryonic masses for DD0 154 in Section 2.8 ( $\sim 3.84 \times 10^8 M_\odot$ ). This is not surprising since the dark matter component is dominant in dwarf galaxies. From Equation (8), the fitted values for  $\tau$  and  $\kappa$  are  $\tau \approx 1.13$  and  $\kappa \approx 0.62$ .

## 5. SUMMARY AND CONCLUDING REMARKS

In Section 2, we examined the rotation curve data of eight galaxies from THINGS (de Blok et al. 2008), and we searched for universal behavior for the function  $\rho(\phi)$ . We found

**Table 1**  
Summary of Estimates for  $m/T$  in the Halos of Eight Galaxies

Galaxy	Distance (Mpc)	$R_{\text{disk}}$ (kpc)	$-(d \log \rho / d\phi)$ (eV K $^{-1}$ )	$m/T$ (Boltzmann Fit) (eV K $^{-1}$ )
NGC 2841	14.1	3.5	190 ( $7 \leq r \leq 22$ kpc)	205 ( $7 \leq r \leq 22$ kpc)
NGC 5055	9.2	3.622	440 ( $10 \leq r \leq 25$ kpc)	300 ( $10 \leq r \leq 25$ kpc)
NGC 7331	14.2	3.2	260 ( $8 \leq r \leq 16$ kpc)	225 ( $8 \leq r \leq 16$ kpc)
NGC 2403	4.3	2.7	1100 ( $3 \leq r \leq 10$ kpc)	1140 ( $3 \leq r \leq 10$ kpc)
NGC 2903	9.4	3.0	490 ( $3 \leq r \leq 9$ kpc)	580 ( $3 \leq r \leq 9$ kpc)
NGC 3521	12.2	3.3	380 ( $7 \leq r \leq 15$ kpc)	370 ( $7 \leq r \leq 15$ kpc)
NGC 3198	14.1	4.0	820 ( $5 \leq r \leq 25$ kpc)	800 ( $5 \leq r \leq 20$ kpc)
DD0 154	4.2	0.8	8600 ( $1.5 \leq r \leq 6.5$ kpc)	7500 ( $1.5 \leq r \leq 6.5$ kpc)

**Notes.** The second column lists the distances to the galaxies used in this article. The third column quotes the distance scale of the disks from Mannheim & O’Brien (2012). In Column 4 we give the mean values of  $-(d \log \rho / d\phi)$  in regions (indicated below in parenthesis) where the derivatives are approximately constant. The values for  $m/T$  obtained from the fits to the Boltzmann gas (for the region in the parenthesis below) is given in Column 5.

indications that it has an exponential behavior in regions  $R_G \leq r \leq R_{\text{max}}$  of the halos. We modeled the regions with an effective theory in Section 3. The dynamics in the spherical shell  $R_G \leq r \leq R_{\text{max}}$  was described by a self-gravitating isothermal gas, subject to an external gravitational field due to the inner-most region  $r \leq R_G$ . General solutions are specified by two dimensionless parameters, which were denoted by  $\tau$  and  $\kappa$ , while three dimensionfull parameters are required for a fit to the data. From typical rotation velocities, we checked that the (dark matter) particles responsible for flat rotation curves move nonrelativistically and that the quantum statistics are negligible in typical regions where the model has application. In Section 4, the rotation curve data was fit to solutions to the model in the regions  $R_G \leq r \leq R_{\text{max}}$  where Boltzmann-like behavior was found. The fits rely on the gravitational attraction to the baryonic matter in the inner region  $r \leq R_G$ , but they do not require any detailed knowledge of the various density profiles; i.e., they do not require the use of mass models.

Our results for the fits and searches for Boltzmann-like behavior of the eight galaxies are summarized in Tables 1 and 2 below. Table 1 contains two different estimates for  $m/T$  for each spherical shell region (Columns 4 and 5), along with distance scales for the various galaxies. The second column of Table 1 lists the distances to the galaxies used in this article, while the third column contains the distance scale of the disks (Mannheim & O’Brien 2012). In Column 4, we give the result for the mean values of  $-(d \log \rho / d\phi)$  in the regions (indicated below in parenthesis), where  $\rho(\phi)$  exhibited exponential behavior. (Recall,  $-(d \log \rho / d\phi)$  is a constant, namely,  $m/T$ , for the Boltzmann gas.) The results were obtained using the eight-parameter series fits of the rotation velocity data described in Section 2. The table shows that the regions exhibiting Boltzmann-like behavior are generally much larger

**Table 2**  
Summary of Mass Estimates and  $(\tau, \kappa)$  for Eight Galaxies

Galaxy	$M_{\text{baryons}}$ ( $10^{10} M_{\odot}$ )	$M(R_G)$ ( $10^{10} M_{\odot}$ )	$M(R_G, R_{\text{max}})$ ( $10^{10} M_{\odot}$ )	$(\tau, \kappa)$
NGC 2841	14.3	17 ( $r \leq 7$ kpc)	29 ( $7 \leq r \leq 22$ kpc)	(0.37, 0.42)
NGC 5055	13.4	10.5 ( $r \leq 10$ kpc)	12.9 ( $10 \leq r \leq 25$ kpc)	(0.55, 0.21)
NGC 7331	19.25	13 ( $r \leq 8$ kpc)	9 ( $8 \leq r \leq 16$ kpc)	(0.50, 0.21)
NGC 2403	0.77	0.59 ( $r \leq 3$ kpc)	3.25 ( $3 \leq r \leq 10$ kpc)	(0.81, 0.67)
NGC 2903	2.06	2.4 ( $r \leq 3$ kpc)	6.3 ( $3 \leq r \leq 9$ kpc)	(0.41, 0.90)
NGC 3521	13.1	8.9 ( $r \leq 7$ kpc)	8.8 ( $7 \leq r \leq 15$ kpc)	(0.39, 0.36)
NGC 3198	4.12	1.9 ( $r \leq 5$ kpc)	8.9 ( $5 \leq r \leq 20$ kpc)	(0.58, 0.59)
DD0 154	0.0384	0.034 ( $r \leq 1.5$ kpc)	0.32 ( $1.5 \leq r \leq 6.5$ kpc)	(1.13, 0.62)

**Notes.** Column 2 lists the total mass baryonic mass of the galaxy, as determined from a mass model (de Blok et al. 2008). In Column 3, we give the value of the mass  $M(R_G)$  in the interior region ( $r \leq R_G$ ), obtained from the fit to the Boltzmann gas. The mass  $M(R_G, R_{\text{max}})$  of the Boltzmann-like region, estimated using Equation (17), appears in Column 4. Column 5 lists the fitted values of the dimensionless parameters  $\tau$  and  $\kappa$ .

than the disk scale. For the examples of NGC 5055, as well as for NGC 2841, these regions are  $\sim 15$  kpc, corresponding to roughly four times the distance scale. Baryonic matter is expected to be subdominant at such distances. Also, the inner boundary  $r = R_G$  of the spherical shell is greater than the disk scale. Thus, dark matter should give the dominant contribution to the total mass density in the spherical shell  $R_G \leq r \leq R_{\text{max}}$ , and it should therefore be responsible for the apparent Boltzmann-like behavior.

As stated above, Column 4 is an estimate of  $m/T$  in the region  $R_G \leq r \leq R_{\text{max}}$  utilizing the eight-parameter fit. Column 5 of Table 1 gives another determination for  $m/T$  in the same region. These values were obtained in Section 4 by making a fit of the rotation curve data to solutions of the equation for a self-gravitating Boltzmann gas. The two different determinations of  $m/T$  are generally in agreement with each other for the eight galaxies. We note that after assuming that the (dark matter) mass  $m$  is a universal constant, we can compare the relative effective temperatures of dark matter in the spherical shells of the eight dark matter halos. We get

$$T_{\text{NGC2841}} > T_{\text{NGC7331}} > T_{\text{NGC3521}} \sim T_{\text{NGC5055}} > T_{\text{NGC2903}} \\ > T_{\text{NGC3198}} > T_{\text{NGC2403}} > T_{\text{DD0154}}.$$

Table 2 reports on the mass estimates for the spherical shell  $R_G \leq r \leq R_{\text{max}}$  and the inner region  $r \leq R_G$ . Table 2 also gives results for the dimensionless parameters  $(\tau, \kappa)$  for the Boltzmann fits. Column 2 lists the sum  $M_{\text{baryons}}$  of all the baryonic contributions to the mass of the galaxy reported in the literature. The disk and bulge contributions were obtained from a mass model in de Blok et al. (2008, ; specifically, the model with fixed values of the mass to luminosity ratio and the diet Salpeter stellar initial mass function), while the H I gas mass estimates come from Walter et al. (2008). Column 3 gives the

result for the mass  $M(R_G)$  in the interior region  $r \leq R_G$  obtained from the Boltzmann fits, while Column 4 lists estimates of the total matter content in the spherical shell  $R_G \leq r \leq R_{\max}$  using Equation (17). The table shows that for the majority of the galaxies, the regions exhibiting Boltzmann-like behavior are at least as massive, if not more, than the reported values for the sum of all the baryonic components of the galaxies. This is another indication that the region is strongly dominated by dark matter. Also, the spherical shells are, in general, more massive than the interior regions  $r \leq R_G$ . Two exceptional cases are NGC 7331 and NGC 3521, where the mass for the spherical shell  $M_{(R_G, R_{\max})}$  is less than  $M_{\text{baryons}}$ . On the other hand, for the case of the dwarf galaxy DD0 154, the region associated with the exponential behavior for  $\rho(\phi)$  is almost 10 times as massive as the baryonic component of the galaxy.

Finally, Column 5 of Table 2 gives the fitted values for the dimensionless parameters  $\tau$  and  $\kappa$  defining the Boltzmann gas. The results vary from one galaxy to another, and they generally differ from the special case of  $(\tau, \kappa) = (1/2, 1/3)$ , which corresponds to an exactly flat rotation curve. As was discussed in the introduction, isothermal behavior is obvious for the ideal case of exactly flat rotation curves. On the other hand, since from Column 5, the results are, in general, not in agreement with the exactly flat solution, the apparent isothermal behavior could not have been guessed from the outset.

We mention a few words about some of the galaxies in THINGS that were not analyzed here. Two galaxies, NGC 2976 and NGC 3627, were not considered at all because they contained too few data points for an eight-parameter fit. NGC 3031 and NGC 4736 may not be ideal candidates because they are reported as having non-circular motions. Also, at sufficient distances from the origin, the former is affected by tidal interactions from other members of the group (the M81 group, for the case of NGC 3031; de Blok et al. 2008). There are other galaxies in the survey with features that may not make them ideal candidates for an analysis of this sort as well, such as NGC 3627, which has a pronounced bar and an asymmetric spiral structure. The data for the remaining five galaxies in the survey did not exhibit any signs of universal behavior after doing the eight-parameter fit used in Section 2. More specifically, we did not find convincing evidence of Boltzmann-like regions from the data for those galaxies.

In summary, from the rotation velocity data for 19 galaxies from THINGS, we found evidence of Boltzmann-like behavior in the halos of eight galaxies, corresponding to approximately 40% of the sample. More specifically, after making the usual assumptions of spherical symmetry and that the rotation curves are generated by circular orbits, we showed that there were substantial regions of the halos where the density decreased exponentially with the gravitational potential. For NGC 2841 and NGC 5055, agreement with Boltzmann-like behavior was found over a distance which was roughly four times the distance scale of the disk, and the relevant regions were estimated to be much more massive than the total baryonic masses of the galaxies. For the case of the dwarf galaxy DD0 154, the region exhibiting exponential behavior for  $\rho(\phi)$  was approximately six times larger than the disk scale and eight times more massive than the baryonic component, indicating that dark matter dom-

inates the region. In all cases, the exponential behavior breaks down at short and large distances. The breakdown at extremely large distances may indicate that the dynamics described by Equation (5) is not valid when densities go below a certain threshold. It is not hard to understand the breakdown at short distances, since the assumptions of symmetry and a single-component gas are not valid approximations close to the disk.

A number of improvements can be performed to the model presented in Section 3 and its fits of galactic halos in Section 4. The most obvious are to drop the assumption of spherical symmetry and to take into account effects of the H I gas present in the halos. Furthermore, one can try to extend the analysis to include the interior region. As densities grow in the interior, it may then be of interest to consider the effect of quantum statistics.

Finally, the fact that we have evidence of some Boltzmann-like behavior in substantial regions of eight galactic halos may not be accidental, as it may signal the presence of (non-gravitational) dark matter self-interactions. Moreover, it is an indication that such interactions could be sufficient in strength and number for the system to settle down to an equilibrium configuration.

We are very grateful to P. Biermann, R. Buta, N. Okada, and J. Reichenbacher for valuable discussions. We are also grateful to Erwin de Blok for providing us with rotation curve data from THINGS. A.S. was supported in part by the DOE, Grant No. DE-FG02-10ER41714.

## REFERENCES

- Ackerman, L., Buckley, M. R., Carroll, S. M., & Kamionkowski, M. 2009, *PhRvD*, **79**, 023519
- Buckley, M. R., & Fox, P. J. 2010, *PhRvD*, **81**, 083522
- Chang, S., Pierce, A., & Weiner, N. 2010, *JCAP*, **01**, 006
- Christodoulou, D. M., & Kazanas, D. 2007, arXiv:0706.3205
- Dave, R., Spergel, D. N., Steinhardt, P. J., & Wandelt, B. D. 2001, *ApJ*, **547**, 574
- de Blok, W. J. G., Walter, F., Brinks, E., et al. 2008, *AJ*, **136**, 2648
- Destri, C., de Vega, H. J., & Sanchez, N. G. 2013, *NewA*, **22**, 39
- Emden, R. 1907, *Gaskugeln: Anwendungen der Mechanischen Warmetheorie auf Kosmologische und Meteorologische Probleme* (Berlin: Teubner)
- Feng, J. L., Kaplinghat, M., & Yu, H.-B. 2010, *PhRvL*, **104**, 151301
- Foot, R., & Volkas, R. R. 2004, *PhRvD*, **70**, 123508
- Frusciante, N., Salucci, P., Vernieri, D., Cannon, J. M., & Elson, E. C. 2012, *MNRAS*, **426**, 751
- Kaplinghat, M., Tulin, S., & Yu, H.-B. 2013, arXiv:1308.0618
- Lin, T., Yu, H.-B., & Zurek, K. M. 2012, *PhRvD*, **85**, 063503
- Liu, F. K. 1996, *MNRAS*, **281**, 1197
- Loeb, A., & Weiner, N. 2011, *PhRvL*, **106**, 171302
- Mannheim, P. D., & O'Brien, J. G. 2012, *PhRvD*, **85**, 124020
- Mishchenko, Y., & Ji, C.-R. 2003, *PhRvD*, **68**, 063503
- Mohapatra, R. N., Nussinov, S., & Teplitz, V. L. 2002, *PhRvD*, **66**, 063002
- Natarajan, P., & Lynden-Bell, D. 1997, *MNRAS*, **286**, 268
- Navarro, J. F., Frenk, C. S., & White, S. D. M. 1997, *ApJ*, **490**, 493
- Oh, S.-H., de Blok, W. J. G., Brinks, E., Walter, F., & Kennicutt, R. C., Jr. 2011, *AJ*, **141**, 193
- Peebles, P. J. E. 1993, *Principles of Physical Cosmology* (Princeton, NJ: Princeton Univ. Press), **718**
- Spergel, D. N., & Steinhardt, P. J. 2000, *PhRvL*, **84**, 3760
- Tulin, S., Yu, H.-B., & Zurek, K. M. 2013a, *PhRvL*, **110**, 111301
- Tulin, S., Yu, H.-B., & Zurek, K. M. 2013b, *PhRvD*, **87**, 115007
- Walter, F., Brinks, E., de Blok, W. J. G., et al. 2008, *AJ*, **136**, 2563